Identification of Human Pathways Acting on Nuclear Non-Coding RNAs Using the Mirror Forward Genetic Approach

Rui Che[1, 2 §], Monireh Panah[1, 2 §], Bhoomi Mirani[1, 2], Krista Knowles[1, 2], Anastacia Ostapovich[3], Debarati Majumdar[1, 2], Xiaotong Chen[1], Joseph DeSimone[1], William White[1], Megan Noonan[1], Hong Luo[1], and Andrei Alexandrov[1, 2 *]

[1]Dept. of Genetics and Biochemistry, Clemson University, Clemson, SC 29631, USA

[2]Clemson University Center for Human Genetics, Greenwood, SC 29646, USA

[3]Dept. of Molecular Biophysics and Biochemistry, Yale University, New Haven, CT 06536, USA

§ authors contributed equally

* correspondence: andreia@clemson.edu

SUMMARY

Despite critical roles in diseases, human pathways acting on strictly nuclear non-coding RNAs have been refractory to forward genetics. To enable their forward genetic discovery, we developed a single-cell approach that “Mirrors” activities of nuclear pathways with cytoplasmic fluorescence. Application of Mirror to two nuclear pathways targeting MALAT1’s 3′ end, the pathway of its maturation and the other, the degradation pathway blocked by the triple-helical Element for Nuclear Expression (ENE), identified nearly all components of three complexes: Ribonuclease P and the RNA Exosome, including nuclear DIS3, EXOSC10, and C1D, as well as the Nuclear Exosome Targeting (NEXT) complex. Additionally, Mirror identified DEAD-box helicase DDX59 associated with the genetic disorder Oral-Facial-Digital syndrome (OFD), yet lacking known substrates or roles in nuclear RNA degradation. Knockout of DDX59 exhibits stabilization of the full-length MALAT1 with a stability-compromised ENE and increases levels of 3′-extended forms of small nuclear RNAs. It also exhibits extensive retention of minor introns, including in OFD-associated genes, suggesting a mechanism for DDX59 association with OFD. Mirror efficiently identifies pathways acting on strictly nuclear non-coding RNAs, including essential and indirectly-acting components, and, as a result, uncovers unexpected links to human disease.

INTRODUCTION

Nuclear-localized long non-coding RNAs (lncRNAs) carrying non-canonical 3′-ends with structured triple-helical Elements for Nuclear Expression (ENEs) (**Fig**. **1a**)[1-4] play critical roles in a variety of human diseases, including cancers[5,6] as well as developmental[7] and viral disorders[8,9]. Overexpression of the abundant, stable, vertebrate-specific, 5′-capped nuclear lncRNA Metastasis Associated Lung Adenocarcinoma Transcript 1 (MALAT1)[1,2,10,11] promotes tumor growth by increasing cell proliferation, invasion, and metastasis. It correlates with poor survival in such prevalent cancers as lung, pancreatic, cervical, colorectal, and others[12-17]. The 3′ end of the nuclear lncRNA MALAT1 is not polyadenylated; instead, it is formed by RNase P cleavage (**Fig**. **1b**) upstream of a tRNA-like RNA structure, mascRNA[18,19]. Since downregulation of MALAT1 RNA levels decreases tumor growth and metastasis and promotes cell differentiation[20,21], this lncRNA represents a promising target for cancer treatment[5,11,21-25]. The ENE-containing human multiple endocrine neoplasia lncRNA[4] (MEN-β, also called NEAT1_2), which is a component of nuclear paraspeckles, has also been implicated in a variety of cancers and diseases[6,26-29].

For each of these lncRNAs, a structured triple-helical ENE element (**Fig**. **1a**) has been shown to protect the 3′ end from nuclear RNA degradation machinery (**Fig**. **1b**) [1-3,30]. This 3′ end-acting nuclear degradation machinery is efficient, as the lncRNAs' half-life and steady-state levels critically depend on the protective function of the intact ENE structure[1,2]: a single-nucleotide destabilizing substitution C8351G within the MALAT1 ENE (**Fig**. **1c**) results in a 20-fold reduction in MALAT1 levels, whereas the deletion of the entire 80-nucleotide ENE element leads to their dramatic 60-fold decrease[19].

Despite the profound effect of nuclear pathways on steady-state levels of nuclear lncRNAs, and despite the major impact of these steady-state levels on human diseases, it is unknown what human nuclear degradation pathways are blocked from degrading nuclear lncRNAs by the 3′ triple-helical ENE elements. The reason such 3′-end targeting human pathways have not been interrogated using forward genetics is due to the strictly nuclear localization of the respective ENE-containing lncRNAs. Whereas forward genetic interrogation must use lncRNA abundance or processing efficiency as quantifiable screening readouts, their quantification can only be achieved in relatively low throughput. This stems from the fact that, unlike mRNAs, nuclear lncRNAs are not exported into cytoplasm and translated, precluding the use of translation-dependent reporter systems.

Such a technological barrier exists not only for the above-mentioned nuclear lncRNAs, but for nearly 30% of all human non-coding RNAs[31] due to their nuclear localization. Due to the lack of robust genome-wide forward genetic approaches, most of our knowledge about human nuclear RNA pathways and their components, including the nuclear RNA exosome and its associated factors[32-34] is derived

from non-genetic approaches and studies in model organisms. This leads to a gap in knowledge about human-specific nuclear pathways and their regulation, contributing to incomplete understanding of human diseases.

We overcame these technological barriers by developing the forward genetic Mirror approach, which we applied to identify components of two human nuclear pathways targeting the 3′ end of MALAT1. One of them is the pathway of 3′ end maturation of MALAT1 and the other is the degradation pathway blocked by the triple-helical ENE stability element. Genome-wide Mirror screening identified numerous components of the three major nuclear RNA-processing complexes: Ribonuclease P (RNase P), the nuclear RNA Exosome, and the Nuclear Exosome Targeting (NEXT) complex, as well as three additional genes: DDX59, C1D, and BRF2. We found that the DEAD box helicase DDX59, which lacked a known substrate or role in nuclear RNA degradation, influences nuclear RNA degradation through an extensive retention of U12 introns within components of the RNA Exosome and the NEXT complex, suggesting a previously unknown function of DDX59 in minor intron splicing. Additional retained U12 introns affect genes associated with the rare genetic developmental disorder Oral-Facial-Digital (OFD) syndrome, suggesting a mechanism for DDX59 association with OFD. We further observe effects of DDX59 on endogenous snRNAs. Collectively, we demonstrate that the Mirror forward genetic approach efficiently identifies components of nuclear pathways acting on human nuclear lncRNAs, revealing surprising connections to human disease.

RESULTS

Design and implementation of the Mirror approach for forward genetic discovery of nuclear factors targeting 3′ end of the human MALAT1. Since translation-dependent reporter systems cannot be used directly for forward genetic interrogation of pathways acting on strictly *nuclear* human lncRNAs, we developed the Mirror approach (**Fig**. **1d**), which relies on nuclear export of a fragment of non-polyadenylated nuclear RNA of interest to produce fluorescence signal. Here, we employed the previously reported finding that a GFP reporter carrying the downstream 3′ triple-helical ENE sequence of MALAT1 or MEN-β can undergo nuclear export and translation into a functional fluorescent protein[2]. We reasoned that inhibition of nuclear pathways acting on a similarly-designed reporter would affect (i.e., be 'mirrored' by) its steady-state cytoplasmic fluorescence, enabling forward genetic screening for components of human nuclear machinery acting on lncRNAs that would otherwise never leave the nucleus. We further reasoned that whereas the genome-wide forward genetic screening using such a Mirror reporter would simultaneously identify components of both nuclear (black) and cytoplasmic

(grey) pathways acting on it (schematically shown in **Fig**. **1d**), subsequent post-screening analysis of the effects of knockout of individual identified genes on the endogenous nuclear lncRNA (**Fig**. **1d**) will distinguish components of nuclear and cytoplasmic pathways, identifying components of nuclear pathways acting on the strictly nuclear lncRNA of interest.

We employed Mirror for the forward genetic identification of two human pathways acting on the 3′ end of the strictly nuclear lncRNA MALAT1: one of them is the pathway of the 3′ end maturation of MALAT1 and the other is the pathway of MALAT1 nuclear degradation that is blocked by the triple-helical ENE element (these two distinct pathways are identified by Mirror simultaneously in a single genetic screen). Each Mirror reporter employs multiple signal- and sensitivity-enhancing features of the previously described single-cell-based dual-color Fireworks system[35]. Similarly to Fireworks, each Mirror reporter expresses a single polyprotein consisting of (1) repeats of fluorescent proteins (GFP or RFP), (2) TEV protease, and (3) β-globin, which contains an intron to improve nuclear export. The proteolytic activity of TEV protease separates fused fluorescent proteins, the protease, and the β-globin to eliminate negative effects on localization, maturation, and the half-life of the fused fluorescent proteins. These features increase the fluorescence signal produced by a single transcription unit of the reporter to improve the sensitivity of the genetic screen[35]. Uniquely, each Mirror reporter (**Figs**. **1e** and **S1a**) carries two elements of the human lncRNA MALAT1: the 3′ ENE stability element and the tRNA-like mascRNA element[18] (**Fig**. **1a-b**). The ENE of one of these reporters carries a single-nucleotide substitution, C8351G (**Figs**. **1a**, **c-e** and **S1a**), introduced to make it more susceptible to nuclear degradation[18,19]. To enhance screening specificity, each individual Mirror cell expresses a second, wild-type ENE control reporter that differs from the stability-compromised ENE by just a single nucleotide (**Figs**. **1e**). The ENE(C8351G)-mascRNA(WT)-containing Mirror reporters (**Fig**. **2a**) yield lower steady-state RNA levels (**Fig**. **2c**) and fluorescence (**Fig**. **2e**) than those containing ENE(WT)-mascRNA(WT). To distinguish the effects of gene knockout on ENE-mascRNA from those on the fluorescent protein moiety of the reporters, and to enhance the rigor of screening and validation, we employed two orthogonal Mirror cell lines. These cell lines, named “Red” and “Green”, have WT ENE and ENE(C8351G) swapped (**Figs**. **1e**, **S1a**, and **S2**).

To identify the nuclear degradation machinery that targets the 3′ end of MALAT1 but is prevented from degrading MALAT1 by its intact triple-helical ENE(WT), we hypothesized that knockout of a component of this degradation machinery (**Fig**. **1c**) would result in a greater increase in the fluorescence of reporters with stability-compromised ENE(C8351G) compared to reporters with ENE(WT) (**Figs**. **1e**, **f** and **S1a**, **b**).

To identify components of the second pathway required for 3′ end maturation of MALAT1, including separation of the tRNA-like mascRNA from the MALAT1 lncRNA precursor (**Fig**. **1b**), Mirror leverages

the enhanced stability – and, as a result, increased fluorescence – of the stability-compromised ENE(C8351G) Mirror reporter upon inhibition of mascRNA cleavage (**Fig**. **2**), which stems from the resulting use of the downstream Bovine Growth Hormone (BGH) cleavage and polyadenylation site (**Fig**. **2a**). Similar disruption of mascRNA cleavage and the resulting switch to BGH-directed polyadenylation produce considerably smaller changes in RNA levels (**Fig**. **2b-d**) and fluorescence of the ENE(WT) reporter. These changes are 2.9-fold and 27-fold for the ENE(WT) and ENE(C8351G), respectively (**Fig**. **2e**). As a result, defects in MALAT1 nuclear 3′-end processing are readily identifiable through their differential effects on fluorescence of the same-cell ENE(C8351G) and ENE(WT) Mirror reporters. We chose HeLa cells for Mirror forward genetic screening of MALAT1-acting human nuclear pathways due to the strong association of steady-state levels of MALAT1 with tumor aggressiveness in cervical cancers[14].

In summary, the Mirror approach is designed to simultaneously identify two nuclear pathways acting on the MALAT1 3′ end. Components of the first—the degradation pathway targeting the 3′ end of MALAT1 but prevented from degrading MALAT1 by its intact triple-helical ENE—are expected to affect degradation of the full-length MALAT1 with the stability-compromised ENE(C8351G). Components of the second—the pathway required for MALAT1 3′-end processing—are expected to affect mascRNA cleavage and, potentially, the levels of the wild-type endogenous MALAT1.

Genome-wide Mirror forward genetic screening for components of two pathways acting on the 3′ end of the human lncRNA MALAT1 enriched numerous components of *nuclear* RNA-processing complexes. Figures 3 and **S1c** show the outcomes of two iterative rounds of CRISPR sgRNA-based forward genetic Mirror screening to simultaneously identify components of two human nuclear pathways targeting MALAT1's 3′ end: one being the pathway of its 3′-end maturation and the other being the degradation pathway blocked by the wild-type ENE element. The screening was conducted in the "Red" and "Green" Mirror cell lines (**Fig**. **1e** and **S1a**) using FACS-based iterative rounds of guide RNA (sgRNA) library enrichment (**Fig**. **3b**) intended to amplify pathway-inhibiting sgRNAs and eliminate stochastic false positives[35]. During the 1st round of screening (**Fig**. **3a** and **S1c**), the Mirror cell lines were transduced with the original lentiviral GeCKO-lentiCRISPR sgRNA library[36] containing 64,751 sgRNAs targeting 18,080 human genes. During the 2nd round of screening (**Fig**. **3a** and **S1c**), the original "Red" and "Green" Mirror cell lines (**Fig**. **1e** and **S1a**) were transduced with the enriched lentiviral sgRNA libraries, which were obtained at the end of the 1st round of screening as shown in **Fig**. **3b**. We expected that sgRNAs targeting each of the two pathways would increase (1) GFP fluorescence of the "Red" MALAT1 Mirror cells (*i.e.*, shift them up, **Figs**. **1f** and **3a**) and (2) RFP fluorescence of the "Green" MALAT1 Mirror cells (*i.e.*, shift them right, **Fig**. **S1b**, **c**). Indeed, distinct

markedly enriched populations of cells appeared in the blue gates, comprising 0.08% and 7.64% of cells (**Fig**. **3a**) and the green gate, comprising 0.024% and 4.53% of cells (**Fig**. **S1c**), after the 1st and 2nd rounds of screening, respectively.

Deep sequencing of sgRNAs in the screening-enriched cell population (0.08% of cells in the blue FACS gate in **Fig**. **3a**) revealed numerous sgRNAs targeting *nuclear* RNA-processing factors (**Fig**. **4a** and **e1**). Indeed, 51 of the top 93 most abundant sgRNAs in the screening-enriched library (**Fig**. **4a**) targeted: (i) 9 out of 10 protein components of the human nuclear RNase P[37]: RPP14, RPP21, RPP30, RPP38, RPP40, POP1, POP4 (RPP29), POP5, and POP7 (RPP20); (ii) 9 out of 11 components of the human RNA Exosome[38]: EXOSC2, EXOSC4, EXOSC5, EXOSC6, EXOSC7, EXOSC8, EXOSC9, EXOSC10, including its nuclear DIS3 (but not the cytoplasmic DIS3L) component[39]; (iii) 2 out of 3 components of the human nuclear NEXT (Nuclear Exosome Targeting) complex[40]: RBM7 and SKIV2L2 (hMTR4); and (iv) the nuclear exosome co-localized RNA-binding protein C1D known for its role in 3′-end processing of 5.8S rRNA[41]. For some of these factors, Mirror identified more than one sgRNA (**Fig**. **4a**), and for others, such as RNase P components RPP14, RPP38, POP7, and POP5, nuclear RNA exosome components EXOSC2, EXOSC7, EXOSC8, EXOSC9, EXOSC10, as well as the exosome-associated C1D and the NEXT complex component SKIV2L2, it identified, among the top 93 sgRNAs, every sgRNA present in the original GeCKO library (**Fig**. **4a** and **Supplemental Data S1**). Additional Mirror-identified and subsequently validated sgRNAs targeted TFIIB-like factor BRF2, known to control initiation of Pol III[42] and the predominantly nuclear DEAD-box helicase DDX59, which has no known substrate in any organism[43,44]. All Mirror-identified factors are summarized in **Figure 4e1**.

Underscoring Mirror's efficiency in identifying *nuclear* factors acting on *nuclear* RNAs using reporter's *cytoplasmic* fluorescence, transduction of sgRNAs targeting the individual Mirror-enriched factors (**Fig**. **4a** and **4e1**) produced specific cell populations with a 2- to 15-fold increase in GFP fluorescence (**Fig**. **4b-y** and **d1**). For all 23 genes shown, only minimal effects are observed on the fluorescence of the same-cell control RFP reporter (**Figs**. **1e** as well as **4b-y** and **d1**). Notably, 21 out of 23 (91%) of these genes are classified as "Common Essential" in the DepMap database[45], demonstrating the Mirror's effectiveness in identifying genes critical for viability.

Corroborating the design, one set of the Mirror-identified factors impacts the 3′-end processing and the levels of the endogenous wild-type MALAT1. Collectively, Mirror correctly identified 9 out of 10 known protein components of RNase P required for MALAT1 3′-end processing (**Fig**. **4a**, **4q-e1**). We hypothesized that the absence of RPP25 (hPOP6) among the RNase P protein components in Mirror results reflects a limitation of forward genetics in detecting redundant factors. Indeed, whereas individual knockouts of RPP25 and RPP25L[46] produced no populations with increased green

fluorescence (**Fig**. **4a1** and **b1**), a simultaneous double knockout of these genes produced such a population (**Fig**. **4c1**), confirming functional redundancy.

Since the GeCKO library lacked sgRNAs targeting the catalytic RNA component of RNase P, RPPH1, identifying it using this library would not have been possible. We demonstrate, however, that not only do sgRNAs targeting protein-encoding genes increase fluorescence in the Mirror system, but also those targeting RNA-encoding genes, as shown by the CRISPR-sgRNA knockout of RPPH1 (**Fig**. **4z**).

We show that knockouts of the RNase P-specific (i.e., not shared with RNase MRP) components impact the levels of the endogenous wild-type lncRNA MALAT1 (**Fig. 4f1**), underscoring the unique ability of the Mirror approach to genetically identify nuclear factors that impact the 3′-end processing and levels of this cancer-associated non-coding RNA.

Corroborating the design, the second set of Mirror-identified complexes and factors impacts the nuclear degradation of the full-length lncRNA MALAT1 with stability-compromised ENE. As shown in **Fig. 4e1**, the second set of Mirror-identified factors is part of the established nuclear RNA-degradation complexes, such as the RNA Exosome and the NEXT complex. However, the predominantly nuclear DEAD-box helicase DDX59 could not be readily assigned to them. Furthermore, nothing is known about the substrate of DDX59 in any organism, nor has it been determined whether this substrate is RNA or DNA[14]. To ascertain how DDX59 affects 3′ end of MALAT1, we first confirmed that DDX59 knockout specifically affects the fluorescence of Mirror reporters with a stability-compromised 3′ ENE(C8351G) and that additional sgRNAs toward DDX59 can replicate this effect. In addition to reproducing an increase in fluorescence (**Fig**. **4f**) in the "Red" Mirror cell line (**Fig**. **1e**, **f**), in which the first step of validation was performed (**Fig**. **4b-d1**), the individual transductions of four distinct DDX59-targeting sgRNAs into the orthogonal "Green" Mirror cell line (**Fig**. **S1a**), in which the ENE(C8351G) and ENE(WT) are swapped, produced an increase in RFP fluorescence without significantly affecting GFP fluorescence (**Fig**. **S1b** and **d-h**). This result confirms that DDX59 knockout specifically influences the fluorescence of Mirror reporters with a stability-compromised ENE, and not the wild-type ENE, and ruled out off-target effects of sgRNAs on the fluorescent protein moiety of the reporters.

To confirm that the effects of DDX59 knockout on fluorescence of stability-compromised Mirror reporters represent an accurate reflection of its effects on nuclear degradation of the RNA of MALAT1 with stability-compromised ENE, we analyzed the degradation of the full-length MALAT1(C8351G) RNA expressed from its own native promoter (**Fig**. **4g1**) following the CRISPR sgRNA-based knockout of DDX59 and the cessation of transcription with actinomycin D. Indeed, knockout of DDX59 (quantified in

Fig. **6g**) results in stabilization of the full-length MALAT1(C8351G) RNA ("red" curve in **Fig**. **4h1**) as compared with non-targeting sgRNA control ("blue" curve in **Fig**. **4h1**). As expected for the same-cell stable control provided by the WT ENE during screening, and in contrast to MALAT1 with the stability-compromised ENE(C8351G), we do not expect, nor we do observe, a major effect of DDX59 knockout on endogenous WT MALAT1 during the same actinomycin D time course or on its steady-state levels (**Fig. S1i, j**).

The stabilizing effect of the DDX59 knockout on full-length MALAT1(C8351G) RNA (**Fig**. **4h1**) parallels the effects observed with knockouts of EXOSC10, SKIV2L2, and RBM7 (quantified in **Fig**. **6g**) for this lncRNA (**Fig**. **4i1-k1**). Since EXOSC10, a catalytic subunit of the nuclear RNA Exosome, as well as RBM7 and SKIV2L2, subunits of the Nuclear Exosome Targeting (NEXT) complex[40], are key constituents of two major established complexes involved in nuclear RNA degradation[47,48], their stabilizing effects corroborate correct identification of these complexes by Mirror. The parallel effects of DDX59 suggest it is also required for the nuclear degradation of stability-compromised MALAT1 through a yet-unidentified mechanism.

DDX59 knockout results in retention of minor (U12) introns, impacting components of the RNA Exosome and NEXT complex. To address the role of DDX59 in the nuclear degradation of stability-compromised lncRNA MALAT1, we analyzed transcriptome-wide effects of DDX59 knockout. Remarkably, knockout of DDX59, rigorously obtained as shown in **Figure 5a**, results in profound retention of minor (U12) spliceosomal introns across numerous genes (**Figs**. **5**, **S3d-i**, **S4**, and **S6**). To illustrate the rigor of the FACS-isolation strategy, we compare the knockout cell population ("KO", red traces) not only to cells transduced with a control guide RNA ("CTRL(-)", blue traces), but also to cells propagated on the same plate as knockout cells but lacking a gene knockout ("Main", green traces). The second control mitigates unintended differences in growth conditions, transduction efficiency, and antibiotic selection, as throughout the entire experiment, the cells of the "KO" and "Main" populations grow together on the same plate until sorted by FACS (**Fig**. **5a**). This retention is more pronounced than that resulting from the knockout of the minor spliceosomal factor ZCRB1[49,50], yet exhibits little to no effect on major (U2) introns (**Figs**. **5**, **S3d-i**, **S4**, and **S6**; also shown for U2 introns of housekeeping genes in **Fig**. **S3a-c**). Importantly, neither the knockout of the Mirror-identified NEXT complex component RBM7, nor the knockout of the exosome component EXOSC10 (quantified in **Fig**. **6g**) shows comparable retention of U12 or U2 introns (**Figs**. **5**, **S3**, **S4**, and **S6**), suggesting that the increase in retained minor introns observed with DDX59 knockout is not due to the stabilization of unspliced transcripts resulting from a deficiency in these complexes. The U12 intron retention is evident not only for DDX59 knockout cells compared to negative control cells transduced with a non-targeting

sgRNA (compare the red "KO" IGV traces with the blue "CTRL-" traces in **Figs**. **5**, **S3d-i**, **S4**, and **S6**) but also for DDX59 knockout cells compared to cells in which the same sgRNA toward DDX59 yielded no FACS-detectable increase in fluorescence (compare the red "KO" IGV traces with the green "Main" traces in **Figs**. **5**, **S3d-i**, **S4**, and **S6**). Quantification of U12 intron retention (**Figs**. **5b-d** and **k-m**, **S4b**, and **S6b**) demonstrates that DDX59 is required for the splicing of a set of human minor introns.

As shown in **Figures 5b-g** and **S4g**, the genes with pronounced DDX59-dependent retention of minor introns include RNA Exosome components EXOSC1, EXOSC2, and EXOSC5, as well as the scaffold component of the Nuclear Exosome Targeting (NEXT) complex, ZCCHC8. Since Mirror screening and its validation have shown that both the RNA Exosome and the NEXT complex are required for the degradation of stability-compromised lncRNA MALAT1(C8351G), inactivation of integral components of these complexes through U12 intron retention (**Figs**. **5b-g** and **S4g**) and subsequent reduction of their protein levels (**Fig**. **S5**) explains the Mirror-identified role of DDX59 in the stabilization of lncRNA MALAT1 with a compromised 3′-end triple-helical ENE structure.

Retention of numerous minor (U12) introns in cilia-related genes provides an explanation for the role of DDX59 in Oral-Facial-Digital syndrome (OFD). Whereas mutations in the DEAD-box helicase DDX59 are known to associate with the rare genetic developmental disorder Oral-Facial-Digital (OFD) syndrome[43,51], the mechanism linking defects in DDX59 to OFD remains unknown. It has been found that nearly 20 genes encoding proteins that either represent components of cilia or influence ciliogenesis are associated with at least 14 classes of OFD[52-54]. However, DDX59 is a notable exception among OFD-associated genes because it lacks known cilia-associated roles[52].

We found that knockout of DDX59 induces retention of U12 introns in mRNAs of genes with established roles in OFD and OFD-associated ciliopathies such as C2CD3, TCTN3, and TMEM107 (**Figs**. **5h** and **k**, **S4b** and **d**), mutations in which are associated with, and have been proposed to be causative for, OFD subtypes OFDXIV, OFDIV, and OFDVI, respectively[52-54]. Additionally, knockout of DDX59 results in retention of U12 introns in DCTN3, OCRL, C2CD3, ARMC9, KATNIP, SFI1, CUL1, ACTR10, CCDC28B, PPP5C, TCTN3, ACTL6A, TMEM107, KIFAP3, RABL2A (**Figs**. **5h-m**, **S3d-i**, and **S4a-f**), all of which are associated with ciliogenesis or cilia assembly[55].

Whereas the knockout of DDX59 produces a major effect on retention of minor (U12) spliceosomal introns, retention of major (U2) spliceosomal introns is virtually unaffected (**Figs**. **5**, **S3**, **S4**, and **S6**). As negative controls, knockouts of the NEXT complex component RBM7 and the exosome component EXOSC10 (quantified in **Fig**. **6g**) do not increase retention of either U12 or U2 introns (**Figs**. **5**, **S3**, **S4**, and **S6**). As a positive control, knockout of ZCRB1 increases retention of U12 introns (**Figs**. **5**, **S3**, **S4**, and **S6**), as expected for a knockout of a known component of the human minor spliceosome[49,50].

Collectively, the DDX59-induced retention of U12 introns in OFD-associated and cilia-related genes provides an explanation for its role in Oral-Facial-Digital syndrome.

Knockout of DDX59 results in the accumulation of 3′-extended precursors of endogenous small nuclear RNAs (snRNAs). Consistent with the Mirror-identified stabilizing effect of DDX59 knockout on the nuclear MALAT1(C8351G), which undergoes non-canonical 3′-end processing by RNase P, lacks a poly(A) tail, and is partially devoid of the protection of the intact 3′-end triple-helical ENE structure, we observe that CRISPR-Cas9 knockout of DDX59 increases the steady-state levels of 3′-extended precursors of several endogenous Sm-class snRNAs (**Fig**. **6a-c**) known to undergo complex non-canonical 3′-end processing and lack poly(A) tails[56,57]. RT-qPCR quantification and IGV traces of RNA-seq performed without poly(A) selection show a 5.3- and 4.1-fold increase in the levels of 3'-extended forms of snRNAs U4atac and U11, respectively (**Fig**. **6d, e**). Consistent with (i) our finding that knockout of DDX59 impacts the function of the RNA Exosome and the NEXT complex via retention of minor (U12) introns in mRNAs of key components of these two complexes (**Figs**. **5e-g** and **S4g**), and (ii) known roles of both complexes in the 3′ end processing of snRNA precursor transcripts[48,58], knockouts of a known minor spliceosome component ZCRB1, RNA Exosome component EXOSC10, and the NEXT complex component RBM7 similarly increase the levels of 3′-extended forms of U4atac, U11 and U4-2 (**Fig**. **6a-c**). Two lines of evidence suggest that the increase in 3′-extended forms of minor spliceosomal snRNAs is not the primary cause of the minor intron retention observed in DDX59 knockout: First, whereas the effects of DDX59, RBM7, EXOSC10, and ZCRB1 knockouts on the levels of 3′-extended forms of U4atac, U11, and U4-2 snRNAs show significant similarities (**Fig**. **6a-c**), only the knockouts of DDX59 and ZCRB1, not those of EXOSC10 or RBM7, result in U12 intron retention (**Figs**. **5** and **S3**, **S4**, and **S6**). Second, whereas DDX59 knockout increases the levels of 3′-extended forms of both minor (U12) and major (U2) spliceosomal snRNAs (**Fig**. **6a-c**), retention of only U12 introns is observed (**Figs**. **5** and **S3**, **S4**, and **S6**). This suggests that inactivation of DDX59 impacts a subset of endogenous human nuclear non-canonical RNAs lacking poly(A) tails in a manner similar to that resulting from the minor spliceosome inactivation and the ensuring impairment of the RNA Exosome and NEXT complex.

The Mirror-identified BRF2 is required for MALAT1-mascRNA processing through expression of the RNA component of RNase P, H1 (RPPH1). To elucidate the effect of BRF2 (**Fig**. **4o** and **e1**) on the 3′ end of MALAT1, we analyzed cleavage of the endogenous wild-type lncRNA MALAT1 (**Fig**. **1b**) using RT-qPCR across the RNase P cleavage site. The quantification revealed a 12-fold increase in unprocessed MALAT1-mascRNA transcript following BRF2 knockout (**Fig**. **6f** and **g**). This defect

parallels a nearly 50-fold increase in RNase P-unprocessed MALAT1 following knockout of RPP21, which is an essential RNase P subunit (**Fig**. **6f** and **g**). Additionally, knockout of BRF2 results in a dramatic 10-fold decrease in the steady-state levels of H1 (RPPH1) RNA (**Fig**. **6f**), the catalytic RNA subunit of human RNase P[59], whereas knockout of RPP21 (**Fig**. **6g**) causes less than a 10% reduction (**Fig**. **6f**). Together, these results demonstrate that BRF2, which controls initiation of human Pol III RNA transcripts[42], is required for expression of Pol III-transcribed H1 RNA, and the loss of the H1 RNA leads to the MALAT1 3′-end processing defect identified by Mirror.

DISCUSSION

We developed the Mirror approach, which enabled forward genetic identification of the human post-transcriptional machinery acting on nuclear non-coding RNAs by employing specialized non-polyadenylated reporters that undergo nuclear export and translation (**Figs**. **1d** and **e**, **S1a**, and **S2**). We demonstrate that the fluorescence signal of the Mirror reporters provides a reliable proxy measurement for processing efficiency and/or abundance of a fused fragment of nuclear non-coding RNA of interest (**Figs**. **2** and **4**), thereby enabling forward genetic screening of strictly nuclear pathways acting on it. Employed to discover two human nuclear pathways acting on the 3′ end of nuclear lncRNA MALAT1 with stability-compromised ENE, Mirror identified nearly all (**Fig**. **4**) components of three major nuclear processing and degradation complexes: RNase P, RNA Exosome, and the NEXT complex. It additionally identified a nuclear exosome-associated factor C1D, TFIIB-like factor BRF2, and the DEAD box helicase DDX59 which previously had no known substrate in any organism or role in nuclear RNA processing and degradation (**Fig**. **4e1**). Since Mirror does not rely on growth metrics and instead detects early changes in cell fluorescence that precedes the onset of the knockout-induced lethality, it efficiently identifies essential genes. Underscoring this feature, 21 of the 23 top genes (i.e., 91%) identified by Mirror (**Fig**. **4e1**) are essential[45]. This comprehensive list, alongside with validation of effects on the endogenous lncRNA by at least one component of each of the three identified complexes (**Fig**. **4i1-k1**) and additional factors (**Figs**. **4h1** and **6f**), demonstrates the effectiveness of Mirror in identifying pathways acting on nuclear non-coding RNAs.

Of the three Mirror-identified genes outside the three major complexes, C1D plays an established role in nuclear RNA degradation as a SKIV2L2- and EXOSC10-interacting partner[41], while BRF2 is involved in the initiation of Pol III transcription[42], a process we confirmed as required for the expression of the RNase P catalytic subunit, RNA H1. Whereas Mirror accurately identified the DEAD box helicase DDX59 as judged by its impact on the degradation of the full-length lncRNA MALAT1(C8351G), the

function of DDX59 remained obscure. Examination of the effects of DDX59 on nuclear RNA degradation revealed that they arise from a previously unknown role of DDX59 in minor intron splicing, as knockout of DDX59 produces extensive retention of U12 introns in components of the RNA Exosome EXOSC1, EXOSC2, and EXOSC5 as well as the NEXT complex component ZCCHC8, with the degree of retention being comparable to or greater than that observed with the knockout of the known minor spliceosome component ZCRB1[49,50]. Whereas retention of U12 introns in key components of the RNA Exosome and NEXT complex could potentially fully account for the observed (i) Mirror-identified stabilization of the full-length lncRNA MALAT1(C8351G) and (ii) increased levels of 3′-extended forms of endogenous Sm-class snRNAs, resulting from DDX59 knockout, an additional to minor intron splicing role of DDX59 in nuclear RNA degradation cannot be ruled out. Although no obvious physical associations of DDX59 with spliceosomes have been reported, such an interaction could be transient, which has been observed for DEAD-box helicases. Alternatively, DDX59 may be required for minor intron splicing through an indirect mechanism that remains to be elucidated; emerging studies continue to reveal unexpected twists in minor intron recognition[49,60]. Mirror's identification of the roles of DDX59 in nuclear RNA degradation and minor intron splicing underscores the advantages of forward genetics in identifying components that impact pathways of interest, independently on whether such components act directly, indirectly, transiently, or are essential.

A new role of DDX59 in minor intron splicing provides a missing link between defects in DDX59 and the rare developmental genetic disorder Oral-Facial-Digital syndrome, which is often associated with intellectual disability[52]. Our finding that DDX59 knockout induces retention of minor introns in TCTN3, TMEM107, and C2CD3, all associated with distinct subtypes of OFD and linked to cilia and ciliogenesis, has revealed a mechanism by which mutations in DDX59 may affect these and potentially other OFD and cilia genes, contributing to this genetic disorder[43]. This mechanism of DDX59 in OFD is supported by several facts: First, deficiencies in cilia genes can cause OFD. Of the nearly 20 genes linked to at least 14 subtypes of OFD, only two, including DDX59, have not been definitively associated with cilia structure or function[52-54]. Second, a disproportionately high number (6%-7.6%) of cilia-related genes harbor U12 introns, compared to an average of 2% of U12-containing genes in the human genome[55], suggesting a greater impact of minor splicing defects. Third, deficiencies in U12 intron splicing, including those caused by mutations in minor spliceosome snRNAs, are known to result in ciliary defects in humans[55]. Fourth, minor spliceosome deficiencies are known to associate with OFD syndrome via mis-splicing of genes affecting primary cilia[61]. Additionally, consistent with the impaired Sonic Hedgehog (SHH) signaling observed in DDX59-associated OFD[43], DDX59 knockout leads to extensive retention of U12 introns in the mRNA of Derlin 2 (**Fig**. **S6**), a factor that mediates the retro-translocation of the SHH protein at the endoplasmic reticulum[43,61,62]. Altogether, our finding of DDX59's

impact on U12 intron splicing suggests that a deficiency in DDX59 may affect as many as 86 known cilia- and SHH-related genes spliced by the minor spliceosome[55,61], contributing to OFD.

As we demonstrate with MALAT1, the Mirror strategy can be applied to more than one nuclear pathway, and may be extended to pathways of degradation, biogenesis, and surveillance of other nuclear non-coding RNAs. It also can be applied to identify human factors required to maintain steady-state levels of disease-associated non-coding nuclear RNAs, including the metastasis-promoting lncRNA MALAT1 itself, for which a search for destabilizing small molecules is underway[25,63]. Inhibition or inactivation of such factors would result in a decrease in levels of MALAT1, providing additional potential targets for cancers with poor survival linked to high MALAT1 levels[12-17]. Mirror's unambiguous identification of the components of the nuclear ribonucleoprotein RNase P (**Fig**. **4**), whose inactivation reduces the steady-state levels of the endogenous wild-type lncRNA MALAT1 (**Fig**. **4f1**), represents the first example of the use of forward genetics to address this challenge.

In summary, the Mirror approach enables forward genetic discovery of components of human nuclear pathways acting on strictly nuclear non-coding RNAs. It efficiently identifies pathways components essential for cell viability, those that act indirectly, and, as a result, uncovers unexpected connections to human disease.

EXPERIMENTAL PROCEDURES

Construction of plasmids. *Mirror reporter plasmids*: The 171-nucleotide sequences (shown in Supplemental Data S2) of the human wild-type and C8351G mutant MALAT1's ENE-mascRNA were amplified using PCR primers MALAT-Fg and MALAT-Rg, listed in Supplemental Data S2, from constructs C-G(WT) βΔ1,2-MALAT1 ENE+A+mascRNA and G-G(C8351G) βΔ1,2-MALAT1 ENE+A+mascRNA[19], kindly provided by Dr. Jessica Brown. Mirror reporter plasmids were constructed by cloning these 171-mers into the unique PspXI restriction site of the Fireworks reporter plasmids pAVA2598[GFP(PTC-)] and pAVA2515[RFP(PTC-)][35] using Gibson cloning, producing Mirror reporter plasmids pAVA2965[GFP-ENE(WT)-mascRNA], pAVA2987[RFP-ENE(WT)-mascRNA], pAVA3000[GFP-ENE(C8351G)-mascRNA], pAVA2995[RFP-ENE(C8351G)-mascRNA]. *Guide RNA-expressing plasmids*: Plasmids expressing two sgRNAs were constructed by PCR-amplifying a 332-nucleotide fragment comprising the Cas9 scaffold and 7SK promoter from pAVA3129 (Supplemental Data S4), using a forward primer for sgRNA1 and a reverse primer for sgRNA2 (sequences in Supplemental Data S3), and cloned into BsmBI-linearized blasticidin-resistant lentiCRISPR vector[36] to express first sgRNA from the U6 promoter and the second sgRNA from 7SK promoter. Plasmids

expressing single guide RNAs (sequences in Supplemental Data S3) were constructed by cloning sgRNA sequences into BsmBI-linearized blasticidin-resistant lentiCRISPR vector[36] using Gibson Assembly (New England Biolabs). The resulting lentiviral sgRNA-expressing constructs for gene knockout were sequences and named as follows: pAVA3250 for RBM7, pAVA3251 for SKIV2L2, pAVA3300 for ZCRB1, pAVA3258 for BRF2, pAVA3259 for RPP21, pAVA3586 for RPPH1, pAVA3318 for EXOSC10, pP18(T)_B9 for C1D, pAVA3791 as sgRNA1 for DDX59, pAVA3796 as sgRNA2 for DDX59, pAVA3317 for as sgRNA3 DDX59, pAVA3794 as sgRNA4 for DDX59, pP18(T)_C3 for EXOSC2, pP18(T)_C11 for EXOSC4, pP18(T)_B12 for EXOSC5, pP18(T)_B11 for EXOSC6, pP18(T)_C4 for EXOSC7, pP18(T)_B1 for EXOSC8, pP18(T)_A7 for EXOSC9, pP18(T)_A5 for DIS3, pAVA3773 for Control(-), pAVA3497 for POP1, pAVA3523 for RPP38, pAVA3545 for RPP29, pAVA3498 for POP5, pAVA3546 for RPP20, pAVA3507 for RPP14, pAVA3573 for RPP30, pAVA3540 for RPP40, pAVA3522 for RPP25, pAVA3548 for RPP25L. *Plasmids expressing full-length MALAT1*: Genomic DNA fragment consisting of (i) 1.2 kb of MALAT1 5′ flanking sequence, (ii) 8.8 kb sequence corresponding to MALAT1 lncRNA, and (iii) 0.7 kb of MALAT1 3′ flanking sequence was PCR-amplified from genomic DNA of the HeLa Fireworks cell line[35], cloned into the BglII and XhoI restriction sites of the pcDNA5/FRT plasmid (Invitrogen) and verified by sequencing. An 11-nucleotide sequence (5′-cgctcgacgta-3′) was inserted 43 nucleotides upstream of the MALAT1 ENE sequence using the NheI restriction site to distinguish exogenously expressed MALAT1 from its endogenously expressed copies. C8351G mutation was introduced into the resulting 10.8 kb construct using PCR mutagenesis with primers listed in Supplemental Data S2. The resulting plasmids pAVA3169(MALAT1(C8351G)) and pAVA3171(MALAT1(WT)) are schematically shown in **Fig. 4g1**. Full sequences of all plasmids are shown in Supplemental Data S4; they will be deposited to the Addgene repository by the time of publication.

Construction of stable cell lines. Stable orthogonal “Red” and “Green” Mirror cell lines shown in **Fig. S2** were obtained by exchanging FRT-integrated Fireworks NMD reporters[35] in the “Green” Fireworks HeLa cell line AVAM526[35] for Mirror reporters using transient co-transfection of pAVA2987 [RFP-ENE(WT)-mascRNA], pAVA3000 [GFP-ENE(C8351G)-mascRNA], pAVA2995 [RFP-ENE(C8351G)-mascRNA], and/or pAVA2965 [GFP-ENE(WT)-mascRNA] with the Flp recombinase-expressing plasmid pOG44 (Invitrogen). Single colonies of cells with stably integrated Mirror reporters were selected using hygromycin (150-300 µg/mL) and puromycin (0.08-0.16 µg/mL). Expanded colonies were FACS-sorted, propagated, and saved as Mirror “Red” AVAM712 (GFP-ENE(C8351G)-mascRNA, RFP-ENE(WT)-mascRNA) and “Green” AVAM742 (GFP-ENE(WT)-mascRNA, RFP-ENE(C8351G)-mascRNA) stable cell lines.

Cell culture and maintenance. The "Red" Mirror cell line was maintained in DMEM (Gibco) media supplemented with 10% fetal bovine serum (FBS, Gibco), 100 U/mL penicillin-streptomycin (Corning), 150 µg/mL hygromycin (InvivoGen), and 0.08 µg/mL puromycin (InvivoGen). The "Green" Mirror cell line was maintained in DMEM media supplemented with 10% FBS, 100 U/mL penicillin-streptomycin, 300 µg/mL hygromycin, and 0.16 µg/mL puromycin. All fluorescent cell lines were routinely FACS-analyzed and sorted for stable GFP and RFP expression. HEK293T cells were maintained in DMEM supplemented with 10% FBS and 100 U/mL Penicillin-Streptomycin. All cell lines are authenticated using Short Tandem Repeat (STR) analysis and confirmed to be mycoplasma-free using PCR-based tests.

Production of lentiviruses and transduction of human cell lines. To produce lentiviruses, sgRNA-expressing LentiCRISPR plasmids, listed in Supplemental Data S3, were co-transfected with the pCMV-dR8.91 packaging and pMD2.G envelope plasmids into the packaging HEK293T cells (AVAM761) using the TransIT-293 Transfection Reagent (Mirus Bio). Following daily media changes (DMEM, 30% FBS, 100 U/mL penicillin-streptomycin), lentivirus-containing media was collected 48 and 72 hours post-transfection, centrifuged at 900 g for 6 minutes to remove cellular debris, passed through a 0.45 µm filter, supplemented with 15 µg/mL polybrene (Millipore Sigma), and added to the Mirror cell lines growing at about 40% confluency. Selection for blasticidin-expressing infected cells was performed for 3 to 4 days using 3.0 µg/mL blasticidin (InvivoGen), which was added on the 3rd day post-infection.

Forward genetic screening using the Mirror approach. A single biological screen was performed in which total of $5x10^7$ cells (2 × 15 cm plates) of the "Red" "Mirror" cell line were transduced with blasticidin-resistant GeCKO-lentiCRISPR[36] viral library and propagated in DMEM media supplemented with 10% FBS, 150 µg/mL hygromycin, 0.08 µg/mL puromycin and 3.0µg/mL blasticidin, with the blasticidin removed 4 days post-infection. Cell populations with increased fluorescence were FACS-isolated 10-11 days post-infection by sorting 360 million cells using the Bio-Rad S3e cell sorter, resulting in the screening each of the 64,751 sgRNAs in the GeCKO library[36] on average 5,800 times. In FACS sorting and analysis, the gates were applied to exclude cell debris [SSC(area) vs FSC(area)], and cell doublets [FSC(width) vs FSC(hight)] (Supplemental Data S6). FACS data were collected using 488 nm and 561 nm excitation and 525/30 and 586/25 emission filters, for GFP and RFP fluorescence channels, respectively. The FACS-isolated cells were pelleted by centrifugation for 10 minutes at 1000g and frozen. Genomic DNA was isolated from FACS-isolated cells using phenol extraction. Sequences

of guide RNAs were amplified from genomic DNA in two steps. First, a linear[64] sgRNA amplification was performed using Herculase II DNA polymerase using 13 thermal cycles with a single sgRNA promoter-specific primer, RandomF (sequences of all primers are listed in Supplemental Data S2), and the following cycling parameters: 96°C 20s, 63°C 1min, 72°C 90s. Then, the second PCR primer, RandomR, was added to the reaction and a regular PCR was performed for 35 cycles as follows: 96°C 3min; 35 cycles of 96°C 20s, 63°C 1min, 72°C 45s; 72°C 10min; 4°C. The PCR-amplified pools of sgRNAs were Illumina-sequenced and/or cloned into a BsmBI-linearized, blasticidin-resistant lentiCRISPR vector[36] to create an enriched lentiCRISPR sgRNA library for subsequent forward genetic screening rounds, as illustrated in **Fig. 3b**. The FACS-screening-enriched pool of sgRNAs and the pool of sgRNAs in the original GeCKO-lentiCRISPR library used for viral transduction were Illumina-sequenced. For each sgRNA in these pools, the enrichment coefficient was calculated as the ratio of sgRNA abundances after and before the screening. sgRNAs with low abundance in the original GeCKO-lentiCRISPR library (read count below 100) were excluded from ranking (Supplemental Data S1). Processing of deep sequencing data was performed as previously described[36].

In vivo analysis of RNA degradation using Actinomycin D. FACS-isolated cell populations of lentivirally-transduced cells expressing Cas9 and gene-specific sgRNAs (pAVA3317 targeting DDX59, pAVA3250 targeting RBM7, pAVA3251 targeting SKIV2L2, pAVA3318 targeting EXOSC10, and pAVA3773 representing negative control; sequences are provided in Supplemental Data S3) were seeded on 10 cm plates at 30% confluency. Eighteen hours later, each plate was transfected using TransIT-293 Transfection Reagent with 18 µg of the plasmid (pAVA3169, full sequence provided in Supplemental Data S4) expressing full-length lncRNA MALAT1 driven by its own promoter and carrying the ENE-destabilizing C8351G mutation. Twenty-four hours post-transfection, the cells were transferred to 6-well plates, recovered for 3 hours, and treated with 5 µg/mL of Actinomycin D for 0, 1, 2, and 3 hours, after which they were lysed using the TRIzol reagent and stored at -80°C for subsequent RNA purification. RNA was purified using TRI reagent (Zymo Research) according to manufacturer's protocol and subjected to two 15-minute rounds of DNase I (Promega) treatment, phenol extraction, and ethanol precipitation. RT-qPCR quantification of RNA levels was performed as described below.

RT-qPCR quantification of RNA levels. For each sample, 1 µg of total RNA was reverse-transcribed using iScript™ Reverse Transcription Supermix according to the manufacturer's protocols. The resulting cDNA was diluted 20 times and qPCR-analysed using Applied Biosystems' SYBR Green PCR Master Mix according to the manufacturer's instructions for the CFX Opus 384 system and the following cycling conditions: 95°C for 3 min; 40 cycles of 95°C for 15 sec, 60°C for 30 sec. Relative quantification

of transcript levels was performed using the ΔΔCT method and 18S RNA levels as the reference. Sequences of all primers are listed in Supplemental Data S2.

Western blotting. Western blot of whole-cell lysates from CRISPR-knockout and control cells (obtained as shown in **Fig**. **5a**; DDX59 mRNA knockout levels are shown in **Fig**. **6g**) was performed by boiling samples in 2xLaemmli Sample Buffer (Bio-Rad), resolving them using 4-15% Criterion Precast Gels (Bio-Rad), transferring to Odyssey nitrocellulose membrane (Li-Cor) using TRIS-Glycine buffer (Bio-Rad) supplemented with 20% methanol, blocking the membrane with 5% non-fat dry milk in Tris Buffered Saline-Tween (Boston Bioproducts) for 2 hours at room temperature, incubating with an antibody (overnight at 4C for primary and two hours at room temperature for secondary) in blocking solution, developing using WesternBright ECL kit (Advansta), and imaging using G:Box iChemi XR5 (Syngene). Antibodies are described in Supplemental Data S5.

Analysis of RNase P processing of the endogenous full-length lncRNA MALAT1. The levels of RNase P-unprocessed endogenous full-length lncRNA MALAT1 were measured by RT-qPCR using nested primers across the RNase P cleavage site of MALAT1-mascRNA. RNA extraction and reverse transcription were performed as described above. To quantify the unprocessed MALAT1 transcript, 20 pre-amplification cycles with outside primers (JD08-F and JD08-R; sequences in Supplemental Data S2) were conducted using Applied Biosystems' SYBR Green PCR Master Mix with the PCR cycling parameters: 95°C for 3 min, followed by 20 cycles of 95°C for 15 s, and 60°C for 30 s. Each resulting pre-amplification reaction was diluted 40-fold with water and then used as a template for the subsequent qPCR reaction, which employed inside primers (JD07-F and JD07-R; sequences in Supplemental Data S2) and utilized Applied Biosystems' SYBR Green PCR Master Mix with the PCR cycling parameters: 95°C for 3 min, followed by 40 cycles of 95°C for 15 s, and 60°C for 30 s. The levels of unprocessed MALAT1-mascRNA RNA were normalized to 18S RNA; ΔΔCt was used to quantify the relative expression levels. Data are presented as means of two biological x four technical replicates; error bars represent standard deviation. Statistically significant differences between knockout and control samples were determined by one-way ANOVA. Posthoc comparisons using Tukey's HSD test were conducted to determine the overall difference between groups, and labeled as "*", $P<0.05$; "**", $P<0.01$; "***", $P<0.001$. Positions of qPCR primers are indicated and their sequences are listed in Supplemental Data S2.

RNA-Seq and genome mapping. Extracted RNA was diluted to 50ng/μl and sent for cDNA library construction (without the use of poly(A) selection) and paired-end sequencing (100-bp paired-end

reads) following the manufacturer's protocols (BGI-America, San Jose, CA). 60 millions clean reads received for each sample were mapped to human genome assembly GRCh38.p14 (GCA_000001405.29) using STAR[65] (version 2.7.10b) with BAM output sorted by coordinate and standard output attributes. The resulting alignments were indexed using SAMtools[66] (Version 1.18) and examined using IGV[67] (version 2.16.1).

DATA AVAILABILITY

The high-throughput sequencing data generated in this study, including CRISPR sgRNA library screening datasets, and RNA-Seq datasets have been deposited in NCBI Sequence Read Archive (SRA), accession number: PRJNA1186702. Source data are provided with this paper.

ACKNOWLEDGMENTS

We thank Suzanne DeGregorio and Elizabeth Greif for help with cloning as well as Drs. Joan A. Steiz, David F. Clayton, Kazimierz Tycowski, and Raul Jobava for critical comments on the manuscript. This work was partially supported by funding to Joan A. Steitz from the Howard Hughes Medical Institute, and by National Institutes of Health grants HG009362 and GM139769 (project 1) to Andrei Alexandrov.

COMPETING INTERESTS

The authors declare no competing interests.

FIGURE LEGENDS

Figure 1. Schematics of the pathways acting on the 3′ end of MALAT1 and the Mirror approach to identify them. a. Crystal structure (PDB ID: 4PLX)[1,19] of MALAT1 triple-helical ENE stability element that protects the 3′ end of MALAT1 against nuclear degradation pathways. Position of the ENE-destabilizing mutation C8351G[18] used in this study is indicated by the red arrow. The image is made using Mol* Viewer[68]. **b.** Schematics of the MALAT1 3′-end formation by RNase P cleavage of the tRNA-like mascRNA structure and formation of the triple-helical ENE structure[1,18,19] that protects the 3′ end of MALAT1 against nuclear degradation pathways. **c.** The stability-compromised ENE(C8351G) structure

provides only partial protection against nuclear degradation pathways. **d.** Schematics of the Mirror concept for identifying nuclear pathways acting on nuclear long non-coding lncRNAs using reporters utilizing cytoplasmic fluorescence. **e.** The "Red" Mirror reporter cell line for simultaneous identification of two nuclear pathways acting on the MALAT1 3′ end: the first, a degradation pathway targeting the 3′ end of MALAT1 but prevented from degrading MALAT1 by its intact triple-helical ENE; and the second, the pathway required for MALAT1 3′-end processing. Major sensitivity-enhancing features of the Fireworks fluorescence amplification system employed by Mirror are described[35]. The 3′ end of the MALAT1 ENE Mirror reporters is formed by RNase P cleavage upstream of mascRNA, as indicated by the orange arrow. Steady-state levels of the MALAT1 ENE Mirror reporters depend on the (1) integrity of their 3′-end triple-helical ENE stability element, which is inserted after the β-globin 3′ UTR and can be disrupted by a single nucleotide substitution C8351G (shown in red). In addition to the "Red" Mirror cell line shown here, an orthogonal "Green" reporter cell line (shown schematically in **Figs**. **S1a** and **S2**) provides controls for cell line- and fluorescent protein-specific effects during genome-wide forward genetic screening and candidate gene validation. **f.** Anticipated effects of inhibiting pathways of nuclear degradation and processing on the fluorescence of "Red" Mirror cell line.

Figure 2. The Mirror reporters enable forward genetic identification of human factors required for MALAT1 processing at the ENE-mascRNA junction. a. Schematic of the effect of RNase P cleavage defect on fluorescence of the Mirror reporter. Low RNA levels of the RNase P-processed MALAT1(C8351) Mirror reporter result from a stability-compromising mutation (highlighted in red) within its 3′ ENE, leading to low GFP fluorescence. Inhibition of mascRNA cleavage causes a switch to the downstream Bovine Growth Hormone (BGH) cleavage and polyadenylation site, increasing stability and thus GFP fluorescence of the Mirror reporter, enabling identification of human factors required for MALAT1 3′-end processing. **b.** RT-qPCR quantification of RNase P processing of Mirror reporter variants shown in panels d and e. Values are expressed relative to the RNase P-unprocessed Mirror-ENE(WT)-mascRNA(WT) transcript levels. ΔΔCt was used to quantify the relative expression levels. Data are presented as means of two biological x four technical replicates; error bars represent standard deviation. Statistically significant differences between knockout and control samples were determined by one-way ANOVA. Posthoc comparisons using Tukey's HSD test were conducted to determine the overall difference between groups, and labeled as "*", $P<0.05$; "**", $P<0.01$; "***", $P<0.001$. Sequences of qPCR primers are listed in Supplemental Data S2. **c.** RT-qPCR quantification of steady-state RNA levels of Mirror reporter variants (shown in panels d and e) transiently transfected in HEK293T cells. RNA levels were normalized to blasticidin S resistance (bsr)[69] mRNA expressed from a co-transfected control plasmid. All qPCR statistical tests for panels c were performed as described for panel b; qPCR

primers are listed in Supplemental Data S2. **d.** Sequences and mutations in ENE-mascRNA regions of Mirror reporters shown in panels a, b, c, and e. Substitutions that destabilize ENE (C8351G)[19] or disrupt RNase P cleavage (mut 8356-8370) at the ENE-mascRNA junction are highlighted in red. **e.** Fluorescence of transiently transfected Mirror reporters visualized using Olympus IX70 fluorescence microscope and FACS analysis of the fluorescence of FRT site-incorporated Mirror reporters carrying 3′-end variants schematically shown to the right (nucleotide substitutions are detailed in panel d).

Figure 3. Iterative forward genetic Mirror screening to identify factors required for MALAT1 3′-end processing, as well as factors blocked from degrading MALAT1 by its triple-helical 3′-end ENE element. a. Genome-wide iterative FACS-based forward genetic screening in the "Red" (**Fig**. **1e**) Mirror reporter cell line (analogous screening in the orthogonal "Green" Mirror cell line is shown in **Fig**. **S1c**). **b.** Schematics of iterative forward genetics screening rounds employed in panel a and **Fig**. **S1c**.

Figure 4. Mirror-identified components of human nuclear pathways acting on MALAT1's 3′-end and their validation. a. sgRNAs and their gene targets ranked by their abundance in the Mirror screening-enriched library. Components of RNase P, RNA Exosome, and the NEXT complex are highlighted in green, blue, and orange, respectively. Three additional Mirror-identified and validated below genes – DDX59, C1D, and BRF2 – are shown in purple. **b-y** and **d1.** Validation of Mirror-identified sgRNAs in the "Red" MALAT1 Mirror cell line, which was transduced with individual sgRNAs and analyzed by FACS as described in Materials and Methods. **z-d1.** Validation of additional components of Mirror-identified nuclear complexes. **e1.** Schematics of Mirror-identified complexes acting on the 3' end of MALAT1. Mirror-identified complex components are highlighted consistent with their coloring in panel a. **f1.** RT-qPCR analysis of the effects of knockouts of the RNase P-specific components (i.e., not shared with RNase MRP), RPP21 and RPPH1, on the levels of the endogenous wild-type lncRNA MALAT1. For RT-qPCRs, RNA levels were normalized to 18S RNA; $\Delta\Delta$Ct was used to quantify the relative expression levels. Data are presented as means of two biological x four technical replicates; error bars represent standard deviation. Statistically significant differences between knockout and control samples were determined by one-way ANOVA. Posthoc comparisons using Tukey's HSD test were conducted to determine the overall difference between groups, and labeled as "*", $P<0.05$; "**", $P<0.01$; "***", $P<0.001$. Sequences of qPCR primers are listed in Supplemental Data S2. **g1.** Schematics of the full-length lncRNA MALAT1(C8351G) driven by its own promoter, followed by its own 3′-flanking sequence, and carrying an insertion of 11 nucleotides in a non-conserved region to distinguish it from endogenously-expressed MALAT1 using RT-qPCR. **h1-k1**. Knockouts of Mirror-identified DDX59, RBM7, SKIV2L2, and EXOSC10 inhibit degradation of the full-

length lncRNA MALAT1 with a stability-compromised ENE(C8351G). RT-qPCR-derived MALAT1(C8351G) levels were normalized to 18S RNA and are shown relative to the time of Actinomycin D addition. ΔΔCt was used to quantify the relative expression levels. Data are presented as means of two biological x four technical replicates; error bars represent standard deviation.

Figure 5. DDX59 is required for the proper splicing of U12 introns; its deficiency disrupts the RNA exosome, the NEXT complex, and genes crucial for Oral-Facial-Digital syndrome (OFD) and ciliary function. a. Schematics of generating knockout (KO), Main, and CTRL(-) populations for RNA-seq analysis, in which respective traces are colored in red, green, and blue. These knockouts are rigorously controlled for growth conditions, transduction efficiency, and antibiotic selection, as, throughout the entire experiment, the cell populations grow together on the same plate until sorted by FACS. The IGV tracks are shown only as an illustration of color-coding that is further used in **Figs. 5b-m, 6a-e, S3, S4,** and **S6**. **b-d.** RT-qPCR quantification of intron retention in mRNAs of the exosome components EXOSC1 and EXOSC2 as well as the scaffold component of the Nuclear Exosome Targeting (NEXT) complex, ZCCHC8 after DDX59 knockout as described in panel a. **e-j.** Integrated Genome Viewer (IGV) traces of RNA-seq reads for minor intron-containing genes, the exosome components EXOSC1 and EXOSC2, as well as the scaffold component of the Nuclear Exosome Targeting (NEXT) complex, ZCCHC8, and genes associated with ciliary function, DCTN3 and OCRL, as well as C2CD3, which is also associated with Oral-Facial-Digital (OFD) syndrome. Cell populations with DDX59, RBM7, ZCRB1, and EXOSC10 knockouts were obtained as shown in panel a and their respective IGV traces are colored accordingly. Major and minor introns are labeled as U2 and U12, respectively. **k-m.** RT-qPCR quantification of intron retention in mRNAs of genes associated with ciliary function, DCTN3 and OCRL, as well as C2CD3, which is also associated with Oral-Facial-Digital (OFD) syndrome. For RT-qPCRs, RNA levels were normalized to 18S RNA; ΔΔCt was used to quantify the relative expression levels. Data are presented as means of two biological x four technical replicates; error bars represent standard deviation. Statistically significant differences between knockout and control samples were determined by one-way ANOVA. Posthoc comparisons using Tukey's HSD test were conducted to determine the overall difference between groups, and labeled as "*", $P<0.05$; "**", $P<0.01$; "***", $P<0.001$. Positions of qPCR primers are indicated and their sequences are listed in Supplemental Data S2.

Figure 6. Knockout of DDX59 results in the accumulation of 3′-extended precursors of endogenous snRNAs. a-c. Integrated Genome Viewer (IGV) traces of RNA-seq (performed without poly(A) selection) are shown for minor spliceosomal snRNAs, U4atac and U11 (panels a and b), and for

a major spliceosomal snRNA, U4 (panel c). Cell populations with knockouts of DDX59, RBM7, ZCRB1, and EXOSC10 were obtained as shown in **Fig**. **5a**; their respective IGV traces are colored accordingly.**d-e.** RT-qPCR quantification of the levels of 3′-extended forms of minor spliceosomal snRNAs U4atac (panel d) and U11 (panel e). **f.** RT-qPCR analysis of the effects of BRF2 knockout on (i) processing of the endogenous full-length lncRNA MALAT1 by RNase P and (ii) RNA levels of its catalytic component RNA H1. The left graph shows analysis of cleavage across the RNase P site of the endogenous full-length lncRNA MALAT1, and the right graph shows RNA levels of RNA H1 in knockout cell populations. Knockout of RPP21, which is unique for RNase P (and absent in the closely-related RNase MRP) and essential for its function[37], is shown as a positive and negative control in the left and right graphs, respectively. **g.** RT-qPCR quantifications of mRNA levels in cell populations with CRISPR-induced knockouts of indicated genes, obtained as shown in **Fig**. **5a**. All qPCR quantifications and statistical tests were performed as described in the legend of **Fig**. **5**; qPCR primers are listed in Supplemental Data S2.

BIBLIOGRAPHY & REFERENCES CITED

1 Brown, J. A., Valenstein, M. L., Yario, T. A., Tycowski, K. T. & Steitz, J. A. Formation of triple-helical structures by the 3'-end sequences of MALAT1 and MENbeta noncoding RNAs. *Proc Natl Acad Sci U S A* **109**, 19202-19207, doi:10.1073/pnas.1217338109 (2012).

2 Wilusz, J. E. *et al.* A triple helix stabilizes the 3' ends of long noncoding RNAs that lack poly(A) tails. *Genes Dev* **26**, 2392-2407, doi:10.1101/gad.204438.112 (2012).

3 Torabi, S. F. *et al.* RNA stabilization by a poly(A) tail 3'-end binding pocket and other modes of poly(A)-RNA interaction. *Science* **371**, doi:10.1126/science.abe6523 (2021).

4 Sunwoo, H. *et al.* MEN epsilon/beta nuclear-retained non-coding RNAs are up-regulated upon muscle differentiation and are essential components of paraspeckles. *Genome Res* **19**, 347-359, doi:10.1101/gr.087775.108 (2009).

5 Schmitt, A. M. & Chang, H. Y. Long Noncoding RNAs in Cancer Pathways. *Cancer Cell* **29**, 452-463, doi:10.1016/j.ccell.2016.03.010 (2016).

6 Dong, P. *et al.* Long Non-coding RNA NEAT1: A Novel Target for Diagnosis and Therapy in Human Tumors. *Front Genet* **9**, 471, doi:10.3389/fgene.2018.00471 (2018).

7 Schmitz, S. U., Grote, P. & Herrmann, B. G. Mechanisms of long noncoding RNA function in development and disease. *Cell Mol Life Sci* **73**, 2491-2509, doi:10.1007/s00018-016-2174-5 (2016).

8 Tycowski, K. T. *et al.* Viral noncoding RNAs: more surprises. *Genes Dev* **29**, 567-584, doi:10.1101/gad.259077.115 (2015).

9 Conrad, N. K., Mili, S., Marshall, E. L., Shu, M. D. & Steitz, J. A. Identification of a rapid mammalian deadenylation-dependent decay pathway and its inhibition by a viral RNA element. *Mol Cell* **24**, 943-953, doi:10.1016/j.molcel.2006.10.029 (2006).

10 Ji, P. *et al.* MALAT-1, a novel noncoding RNA, and thymosin beta4 predict metastasis and survival in early-stage non-small cell lung cancer. *Oncogene* **22**, 8031-8041, doi:10.1038/sj.onc.1206928 (2003).

11 Gutschner, T., Hammerle, M. & Diederichs, S. MALAT1 -- a paradigm for long noncoding RNA function in cancer. *J Mol Med (Berl)* **91**, 791-801, doi:10.1007/s00109-013-1028-y (2013).

12 Cheng, Y. *et al.* Role of metastasis-associated lung adenocarcinoma transcript-1 (MALAT-1) in pancreatic cancer. *PLoS One* **13**, e0192264, doi:10.1371/journal.pone.0192264 (2018).

13 Gutschner, T. *et al.* The noncoding RNA MALAT1 is a critical regulator of the metastasis phenotype of lung cancer cells. *Cancer Res* **73**, 1180-1189, doi:10.1158/0008-5472.CAN-12-2850 (2013).

14 Yang, L., Bai, H. S., Deng, Y. & Fan, L. High MALAT1 expression predicts a poor prognosis of cervical cancer and promotes cancer cell growth and invasion. *Eur Rev Med Pharmacol Sci* **19**, 3187-3193 (2015).

15 Qiu, M. T., Hu, J. W., Yin, R. & Xu, L. Long noncoding RNA: an emerging paradigm of cancer research. *Tumour Biol* **34**, 613-620, doi:10.1007/s13277-013-0658-6 (2013).

16 Chen, W. *et al.* MALAT1 is a prognostic factor in glioblastoma multiforme and induces chemoresistance to temozolomide through suppressing miR-203 and promoting thymidylate synthase expression. *Oncotarget* **8**, 22783-22799, doi:10.18632/oncotarget.15199 (2017).

17 Malakar, P. *et al.* Long Noncoding RNA MALAT1 Promotes Hepatocellular Carcinoma Development by SRSF1 Upregulation and mTOR Activation. *Cancer Res* **77**, 1155-1167, doi:10.1158/0008-5472.CAN-16-1508 (2017).

18 Wilusz, J. E., Freier, S. M. & Spector, D. L. 3' end processing of a long nuclear-retained noncoding RNA yields a tRNA-like cytoplasmic RNA. *Cell* **135**, 919-932, doi:10.1016/j.cell.2008.10.012 (2008).

19 Brown, J. A. *et al.* Structural insights into the stabilization of MALAT1 noncoding RNA by a bipartite triple helix. *Nat Struct Mol Biol* **21**, 633-640, doi:10.1038/nsmb.2844 (2014).

20 Xu, S. *et al.* Downregulation of long noncoding RNA MALAT1 induces epithelial-to-mesenchymal transition via the PI3K-AKT pathway in breast cancer. *Int J Clin Exp Pathol* **8**, 4881-4891 (2015).
21 Arun, G. *et al.* Differentiation of mammary tumors and reduction in metastasis upon Malat1 lncRNA loss. *Genes Dev* **30**, 34-51, doi:10.1101/gad.270959.115 (2016).
22 Huarte, M. The emerging role of lncRNAs in cancer. *Nat Med* **21**, 1253-1261, doi:10.1038/nm.3981 (2015).
23 Lin, L., Li, H., Zhu, Y., He, S. & Ge, H. Expression of metastasis-associated lung adenocarcinoma transcript 1 long non-coding RNA in vitro and in patients with non-small cell lung cancer. *Oncol Lett* **15**, 9443-9449, doi:10.3892/ol.2018.8531 (2018).
24 Donlic, A. *et al.* Discovery of Small Molecule Ligands for MALAT1 by Tuning an RNA-Binding Scaffold. *Angewandte Chemie (International ed. in English)* **57**, 13242-13247, doi:10.1002/anie.201808823 (2018).
25 Abulwerdi, F. A. *et al.* Selective Small-Molecule Targeting of a Triple Helix Encoded by the Long Noncoding RNA, MALAT1. *ACS chemical biology* **14**, 223-235, doi:10.1021/acschembio.8b00807 (2019).
26 Yu, X., Li, Z., Zheng, H., Chan, M. T. & Wu, W. K. NEAT1: A novel cancer-related long non-coding RNA. *Cell Prolif* **50**, doi:10.1111/cpr.12329 (2017).
27 Nishimoto, Y. *et al.* The long non-coding RNA nuclear-enriched abundant transcript 1_2 induces paraspeckle formation in the motor neuron during the early phase of amyotrophic lateral sclerosis. *Mol Brain* **6**, 31, doi:10.1186/1756-6606-6-31 (2013).
28 Liu, X. *et al.* Long non-coding RNA NEAT1-modulated abnormal lipolysis via ATGL drives hepatocellular carcinoma proliferation. *Mol Cancer* **17**, 90, doi:10.1186/s12943-018-0838-5 (2018).
29 Riva, P., Ratti, A. & Venturin, M. The Long Non-Coding RNAs in Neurodegenerative Diseases: Novel Mechanisms of Pathogenesis. *Curr Alzheimer Res* **13**, 1219-1231 (2016).
30 Mitton-Fry, R. M., DeGregorio, S. J., Wang, J., Steitz, T. A. & Steitz, J. A. Poly(A) tail recognition by a viral RNA element through assembly of a triple helix. *Science* **330**, 1244-1247, doi:10.1126/science.1195858 (2010).
31 Kapranov, P. *et al.* RNA maps reveal new RNA classes and a possible function for pervasive transcription. *Science* **316**, 1484-1488, doi:10.1126/science.1138341 (2007).
32 Weick, E. M. & Lima, C. D. RNA helicases are hubs that orchestrate exosome-dependent 3'-5' decay. *Current opinion in structural biology* **67**, 86-94, doi:10.1016/j.sbi.2020.09.010 (2021).
33 Zinder, J. C. & Lima, C. D. Targeting RNA for processing or destruction by the eukaryotic RNA exosome and its cofactors. *Genes Dev* **31**, 88-100, doi:10.1101/gad.294769.116 (2017).
34 Belair, C., Sim, S. & Wolin, S. L. Noncoding RNA Surveillance: The Ends Justify the Means. *Chemical reviews* **118**, 4422-4447, doi:10.1021/acs.chemrev.7b00462 (2018).
35 Alexandrov, A., Shu, M. D. & Steitz, J. A. Fluorescence Amplification Method for Forward Genetic Discovery of Factors in Human mRNA Degradation. *Mol Cell* **65**, 191-201, doi:10.1016/j.molcel.2016.11.032 (2017).
36 Shalem, O. *et al.* Genome-scale CRISPR-Cas9 knockout screening in human cells. *Science* **343**, 84-87, doi:10.1126/science.1247005 (2014).
37 Wu, J. *et al.* Cryo-EM Structure of the Human Ribonuclease P Holoenzyme. *Cell* **175**, 1393-1404.e1311, doi:10.1016/j.cell.2018.10.003 (2018).
38 Weick, E. M. *et al.* Helicase-Dependent RNA Decay Illuminated by a Cryo-EM Structure of a Human Nuclear RNA Exosome-MTR4 Complex. *Cell* **173**, 1663-1677.e1621, doi:10.1016/j.cell.2018.05.041 (2018).
39 Tomecki, R. *et al.* The human core exosome interacts with differentially localized processive RNases: hDIS3 and hDIS3L. *Embo j* **29**, 2342-2357, doi:10.1038/emboj.2010.121 (2010).
40 Lubas, M. *et al.* Interaction profiling identifies the human nuclear exosome targeting complex. *Mol Cell* **43**, 624-637, doi:10.1016/j.molcel.2011.06.028 (2011).

41 Schilders, G., van Dijk, E. & Pruijn, G. J. C1D and hMtr4p associate with the human exosome subunit PM/Scl-100 and are involved in pre-rRNA processing. *Nucleic Acids Res* **35**, 2564-2572, doi:10.1093/nar/gkm082 (2007).
42 Gouge, J. *et al.* Redox Signaling by the RNA Polymerase III TFIIB-Related Factor Brf2. *Cell* **163**, 1375-1387, doi:10.1016/j.cell.2015.11.005 (2015).
43 Shamseldin, H. E. *et al.* Mutations in DDX59 implicate RNA helicase in the pathogenesis of orofaciodigital syndrome. *Am J Hum Genet* **93**, 555-560, doi:10.1016/j.ajhg.2013.07.012 (2013).
44 Yang, L. *et al.* EGFR and Ras regulate DDX59 during lung cancer development. *Gene* **642**, 95-102, doi:10.1016/j.gene.2017.11.029 (2018).
45 Meyers, R. M. *et al.* Computational correction of copy number effect improves specificity of CRISPR-Cas9 essentiality screens in cancer cells. *Nat Genet* **49**, 1779-1784, doi:10.1038/ng.3984 (2017).
46 Köferle, A. *et al.* Interrogation of cancer gene dependencies reveals paralog interactions of autosome and sex chromosome-encoded genes. *Cell Rep* **39**, 110636, doi:10.1016/j.celrep.2022.110636 (2022).
47 Puno, M. R. & Lima, C. D. Structural basis for MTR4-ZCCHC8 interactions that stimulate the MTR4 helicase in the nuclear exosome-targeting complex. *Proc Natl Acad Sci U S A* **115**, E5506-e5515, doi:10.1073/pnas.1803530115 (2018).
48 Puno, M. R., Weick, E. M., Das, M. & Lima, C. D. SnapShot: The RNA Exosome. *Cell* **179**, 282-282.e281, doi:10.1016/j.cell.2019.09.005 (2019).
49 Li, B. *et al.* RIP-PEN-seq identifies a class of kink-turn RNAs as splicing regulators. *Nat Biotechnol* **42**, 119-131, doi:10.1038/s41587-023-01749-0 (2024).
50 Will, C. L. *et al.* The human 18S U11/U12 snRNP contains a set of novel proteins not found in the U2-dependent spliceosome. *Rna* **10**, 929-941, doi:10.1261/rna.7320604 (2004).
51 Salpietro, V. *et al.* A loss-of-function homozygous mutation in DDX59 implicates a conserved DEAD-box RNA helicase in nervous system development and function. *Hum Mutat* **39**, 187-192, doi:10.1002/humu.23368 (2018).
52 Franco, B. & Thauvin-Robinet, C. Update on oral-facial-digital syndromes (OFDS). *Cilia* **5**, 12, doi:10.1186/s13630-016-0034-4 (2016).
53 Strong, A. *et al.* Expanding the genetic landscape of oral-facial-digital syndrome with two novel genes. *American journal of medical genetics. Part A* **185**, 2409-2416, doi:10.1002/ajmg.a.62337 (2021).
54 Yamada, M. *et al.* IFT172 as the 19th gene causative of oral-facial-digital syndrome. *American journal of medical genetics. Part A* **179**, 2510-2513, doi:10.1002/ajmg.a.61373 (2019).
55 Khatri, D. *et al.* Deficiency of the minor spliceosome component U4atac snRNA secondarily results in ciliary defects in human and zebrafish. *Proc Natl Acad Sci U S A* **120**, e2102569120, doi:10.1073/pnas.2102569120 (2023).
56 Cuello, P., Boyd, D. C., Dye, M. J., Proudfoot, N. J. & Murphy, S. Transcription of the human U2 snRNA genes continues beyond the 3' box in vivo. *Embo j* **18**, 2867-2877, doi:10.1093/emboj/18.10.2867 (1999).
57 Baillat, D. *et al.* Integrator, a multiprotein mediator of small nuclear RNA processing, associates with the C-terminal repeat of RNA polymerase II. *Cell* **123**, 265-276, doi:10.1016/j.cell.2005.08.019 (2005).
58 Hrossova, D. *et al.* RBM7 subunit of the NEXT complex binds U-rich sequences and targets 3'-end extended forms of snRNAs. *Nucleic Acids Res* **43**, 4236-4248, doi:10.1093/nar/gkv240 (2015).
59 Guerrier-Takada, C., Gardiner, K., Marsh, T., Pace, N. & Altman, S. The RNA moiety of ribonuclease P is the catalytic subunit of the enzyme. *Cell* **35**, 849-857, doi:10.1016/0092-8674(83)90117-4 (1983).
60 Bai, R. *et al.* Structure of the activated human minor spliceosome. *Science* **371**, doi:10.1126/science.abg0879 (2021).

61 Iturrate, A. *et al.* Mutations in SCNM1 cause orofaciodigital syndrome due to minor intron splicing defects affecting primary cilia. *Am J Hum Genet* **109**, 1828-1849, doi:10.1016/j.ajhg.2022.08.009 (2022).
62 Huang, C. H., Hsiao, H. T., Chu, Y. R., Ye, Y. & Chen, X. Derlin2 protein facilitates HRD1-mediated retro-translocation of sonic hedgehog at the endoplasmic reticulum. *J Biol Chem* **288**, 25330-25339, doi:10.1074/jbc.M113.455212 (2013).
63 Zablowsky, N. *et al.* High Throughput FISH Screening Identifies Small Molecules That Modulate Oncogenic lncRNA MALAT1 via GSK3B and hnRNPs. *Non-coding RNA* **9**, doi:10.3390/ncrna9010002 (2023).
64 Chen, C. *et al.* Single-cell whole-genome analyses by Linear Amplification via Transposon Insertion (LIANTI). *Science* **356**, 189-194, doi:10.1126/science.aak9787 (2017).
65 Dobin, A. *et al.* STAR: ultrafast universal RNA-seq aligner. *Bioinformatics (Oxford, England)* **29**, 15-21, doi:10.1093/bioinformatics/bts635 (2013).
66 Danecek, P. *et al.* Twelve years of SAMtools and BCFtools. *GigaScience* **10**, doi:10.1093/gigascience/giab008 (2021).
67 Robinson, J. T. *et al.* Integrative genomics viewer. *Nat Biotechnol* **29**, 24-26, doi:10.1038/nbt.1754 (2011).
68 Sehnal, D. *et al.* Mol* Viewer: modern web app for 3D visualization and analysis of large biomolecular structures. *Nucleic Acids Res* **49**, W431-w437, doi:10.1093/nar/gkab314 (2021).
69 Izumi, M. *et al.* Blasticidin S-resistance gene (bsr): a novel selectable marker for mammalian cells. *Experimental cell research* **197**, 229-233, doi:10.1016/0014-4827(91)90427-v (1991).

Figure 1

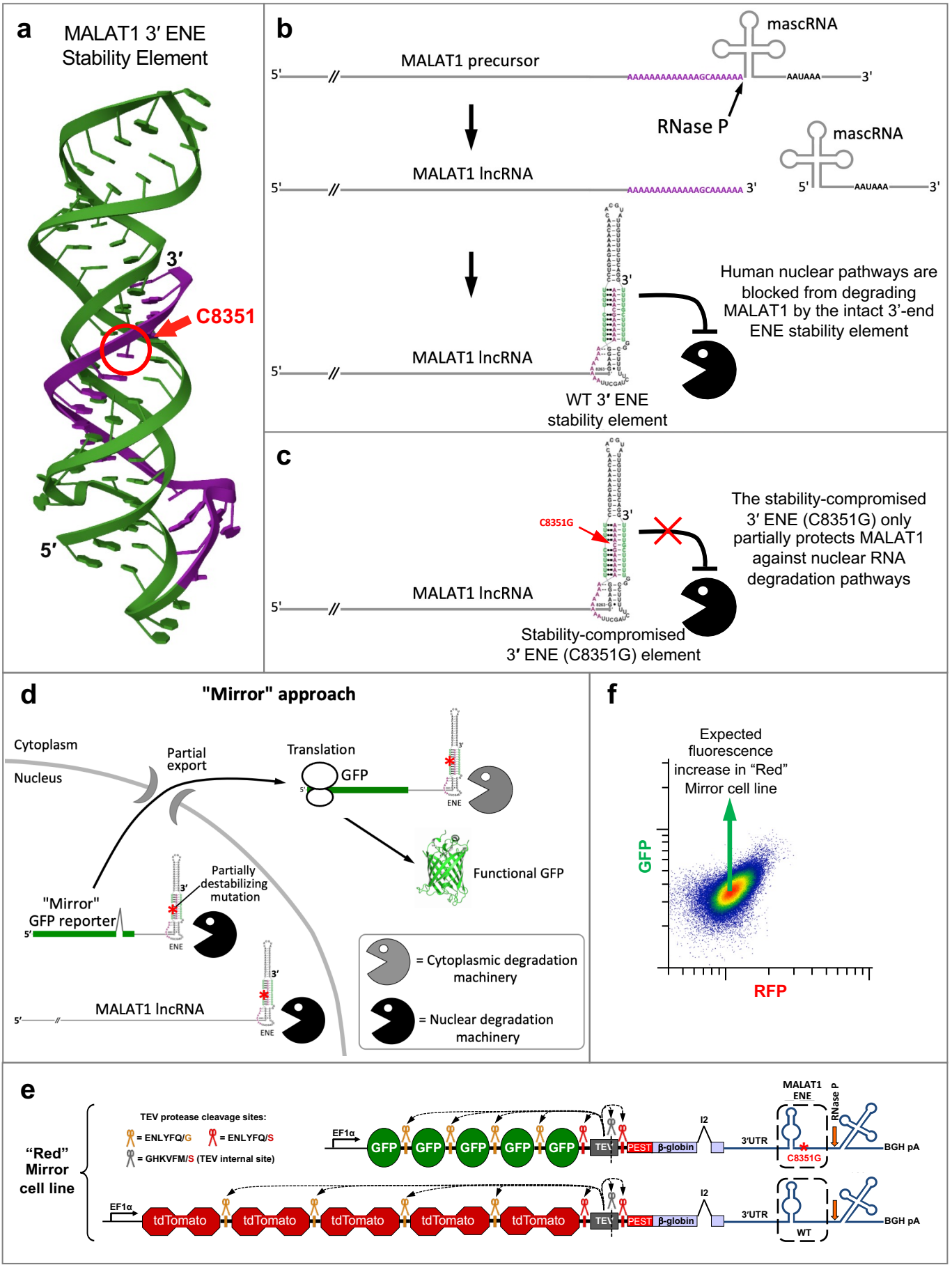
a
MALAT1 3′ ENE Stability Element
3′
C8351
5′
b
mascRNA
MALAT1 precursor
5'
AAAAAAAAAAAAAGCAAAAAA
AAUAAA
3'
RNase P
mascRNA
MALAT1 lncRNA
5'
AAAAAAAAAAAAAGCAAAAAA 3'
5'
AAUAAA
3'
MALAT1 lncRNA
5'
3'
WT 3′ ENE stability element
Human nuclear pathways are blocked from degrading MALAT1 by the intact 3'-end ENE stability element
c
C8351G
3'
MALAT1 lncRNA
5'
Stability-compromised 3′ ENE (C8351G) element
The stability-compromised 3′ ENE (C8351G) only partially protects MALAT1 against nuclear RNA degradation pathways
d
"Mirror" approach
Cytoplasm
Nucleus
Partial export
Translation
GFP
ENE
Functional GFP
Partially destabilizing mutation
"Mirror" GFP reporter
5′
ENE
MALAT1 lncRNA
5′
ENE
= Cytoplasmic degradation machinery
= Nuclear degradation machinery
f
Expected fluorescence increase in "Red" Mirror cell line
GFP
RFP
e
"Red" Mirror cell line
TEV protease cleavage sites:
= ENLYFQ/G
= ENLYFQ/S
= GHKVFM/S (TEV internal site)
EF1α
GFP
TEV
PEST
β-globin
I2
3'UTR
MALAT1 ENE
RNase P
C8351G
BGH pA
tdTomato
WT

Figure 2

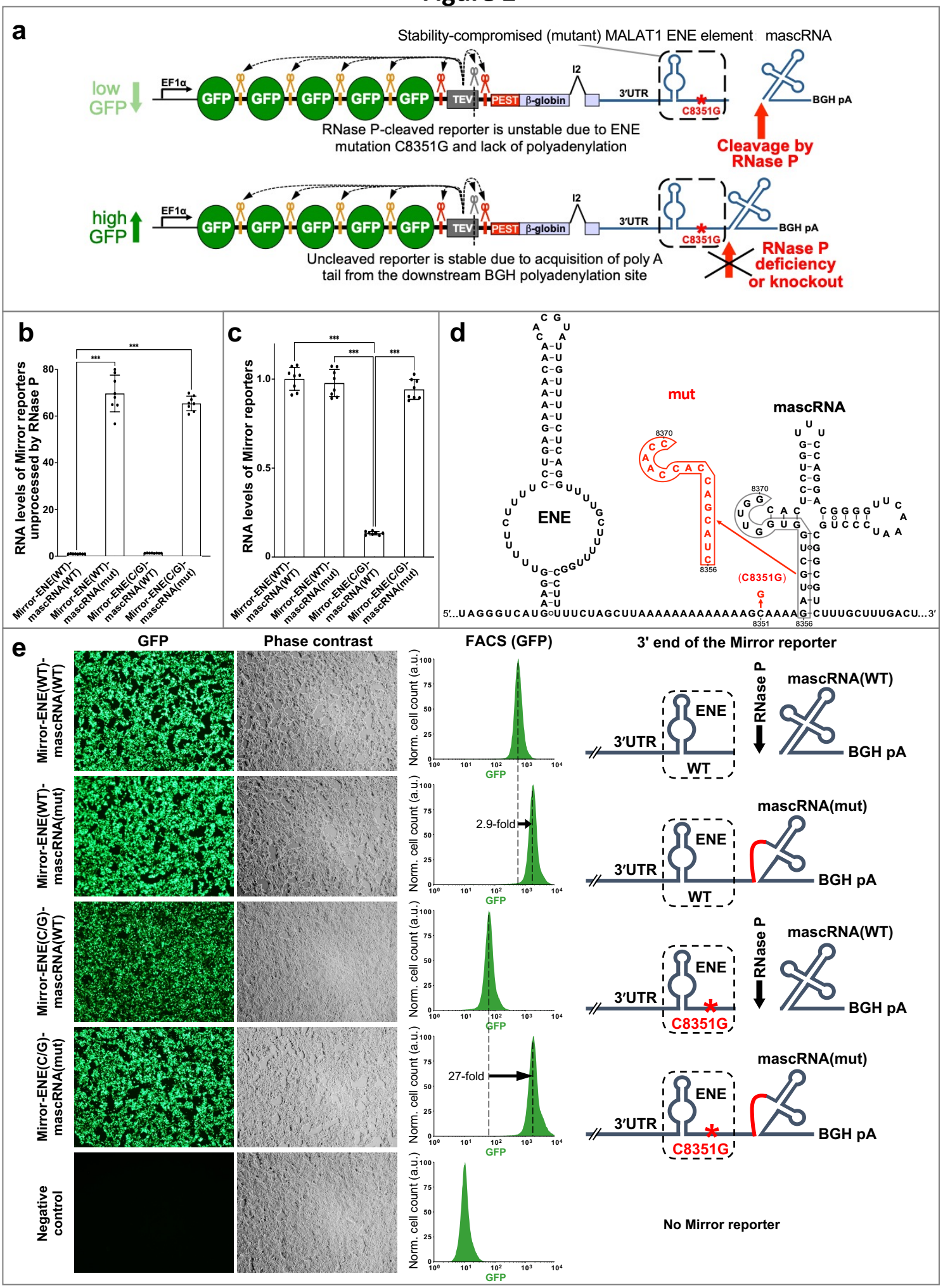
a
Stability-compromised (mutant) MALAT1 ENE element
mascRNA
low GFP
EF1α
GFP
TEV
PEST
β-globin
I2
3'UTR
C8351G
BGH pA
RNase P-cleaved reporter is unstable due to ENE mutation C8351G and lack of polyadenylation
Cleavage by RNase P
high GFP
Uncleaved reporter is stable due to acquisition of poly A tail from the downstream BGH polyadenylation site
RNase P deficiency or knockout
b
RNA levels of Mirror reporters unprocessed by RNase P
Mirror-ENE(WT)-mascRNA(WT)
Mirror-ENE(WT)-mascRNA(mut)
Mirror-ENE(C/G)-mascRNA(WT)
Mirror-ENE(C/G)-mascRNA(mut)
c
RNA levels of Mirror reporters
d
ENE
mut
mascRNA
(C8351G)
5'...UAGGGUCAUGUUUCUAGCUUAAAAAAAAAAAAAGCAAAAGCUUUGCUUUGACU...3'
e
GFP
Phase contrast
FACS (GFP)
3' end of the Mirror reporter
Mirror-ENE(WT)-mascRNA(WT)
Mirror-ENE(WT)-mascRNA(mut)
Mirror-ENE(C/G)-mascRNA(WT)
Mirror-ENE(C/G)-mascRNA(mut)
Negative control
2.9-fold
27-fold
Norm. cell count (a.u.)
RNase P
mascRNA(WT)
mascRNA(mut)
No Mirror reporter

Figure 3

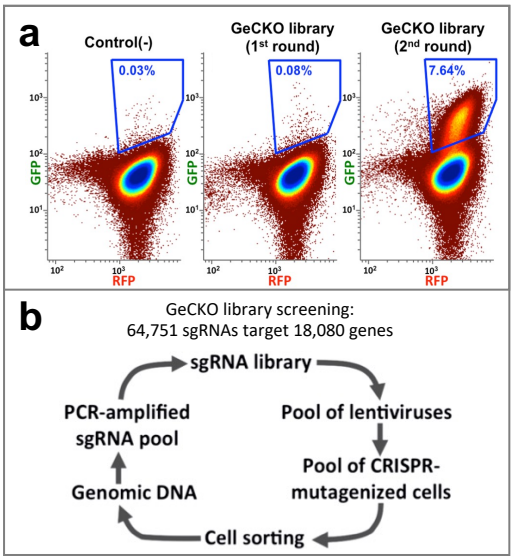
a
Control(-)
GeCKO library (1st round)
GeCKO library (2nd round)
0.03%
0.08%
7.64%
GFP
RFP
b
GeCKO library screening:
64,751 sgRNAs target 18,080 genes
sgRNA library
Pool of lentiviruses
Pool of CRISPR-mutagenized cells
Cell sorting
Genomic DNA
PCR-amplified sgRNA pool

Figure 4

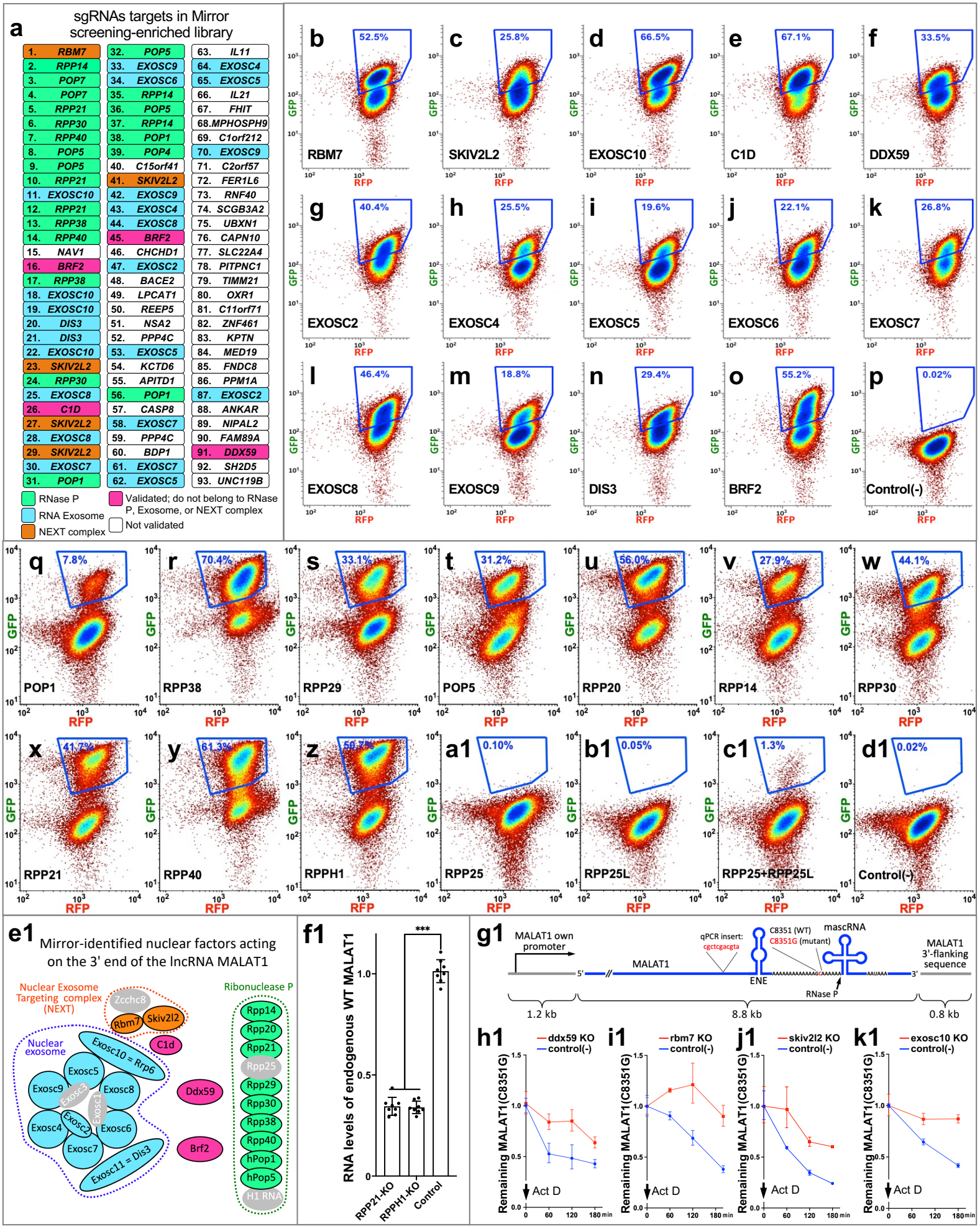
a
sgRNAs targets in Mirror screening-enriched library
1. RBM7
2. RPP14
3. POP7
4. POP7
5. RPP21
6. RPP30
7. RPP40
8. POP5
9. POP5
10. RPP21
11. EXOSC10
12. RPP21
13. RPP38
14. RPP40
15. NAV1
16. BRF2
17. RPP38
18. EXOSC10
19. EXOSC10
20. DIS3
21. DIS3
22. EXOSC10
23. SKIV2L2
24. RPP30
25. EXOSC8
26. C1D
27. SKIV2L2
28. EXOSC8
29. SKIV2L2
30. EXOSC7
31. POP1
32. POP5
33. EXOSC9
34. EXOSC6
35. RPP14
36. POP5
37. RPP14
38. POP1
39. POP4
40. C15orf41
41. SKIV2L2
42. EXOSC9
43. EXOSC4
44. EXOSC8
45. BRF2
46. CHCHD1
47. EXOSC2
48. BACE2
49. LPCAT1
50. REEP5
51. NSA2
52. PPP4C
53. EXOSC5
54. KCTD6
55. APITD1
56. POP1
57. CASP8
58. EXOSC7
59. PPP4C
60. BDP1
61. EXOSC7
62. EXOSC5
63. IL11
64. EXOSC4
65. EXOSC5
66. IL21
67. FHIT
68. MPHOSPH9
69. C1orf212
70. EXOSC9
71. C2orf57
72. FER1L6
73. RNF40
74. SCGB3A2
75. UBXN1
76. CAPN10
77. SLC22A4
78. PITPNC1
79. TIMM21
80. OXR1
81. C11orf71
82. ZNF461
83. KPTN
84. MED19
85. FNDC8
86. PPM1A
87. EXOSC2
88. ANKAR
89. NIPAL2
90. FAM89A
91. DDX59
92. SH2D5
93. UNC119B
RNase P
RNA Exosome
NEXT complex
Validated; do not belong to RNase P, Exosome, or NEXT complex
Not validated
b 52.5% RBM7
c 25.8% SKIV2L2
d 66.5% EXOSC10
e 67.1% C1D
f 33.5% DDX59
g 40.4% EXOSC2
h 25.5% EXOSC4
i 19.6% EXOSC5
j 22.1% EXOSC6
k 26.8% EXOSC7
l 46.4% EXOSC8
m 18.8% EXOSC9
n 29.4% DIS3
o 55.2% BRF2
p 0.02% Control(-)
q 7.8% POP1
r 70.4% RPP38
s 33.1% RPP29
t 31.2% POP5
u 56.0% RPP20
v 27.9% RPP14
w 44.1% RPP30
x 41.7% RPP21
y 61.3% RPP40
z 50.7% RPPH1
a1 0.10% RPP25
b1 0.05% RPP25L
c1 1.3% RPP25+RPP25L
d1 0.02% Control(-)
GFP
RFP
e1
Mirror-identified nuclear factors acting on the 3' end of the lncRNA MALAT1
Nuclear Exosome Targeting complex (NEXT)
Zcchc8
Rbm7
Skiv2l2
C1d
Nuclear exosome
Exosc10 = Rrp6
Exosc5
Exosc9
Exosc3
Exosc8
Exosc1
Exosc4
Exosc2
Exosc6
Exosc7
Exosc11 = Dis3
Ddx59
Brf2
Ribonuclease P
Rpp14
Rpp20
Rpp21
Rpp25
Rpp29
Rpp30
Rpp38
Rpp40
hPop1
hPop5
H1 RNA
f1
RNA levels of endogenous WT MALAT1
***
RPP21-KO
RPPH1-KO
Control
g1
MALAT1 own promoter
MALAT1
qPCR insert: cgctcgacgta
C8351 (WT)
C8351G (mutant)
mascRNA
MALAT1 3'-flanking sequence
ENE
RNase P
1.2 kb
8.8 kb
0.8 kb
h1 ddx59 KO control(-)
i1 rbm7 KO control(-)
j1 skiv2l2 KO control(-)
k1 exosc10 KO control(-)
Remaining MALAT1(C8351G)
Act D
min

Figure 5

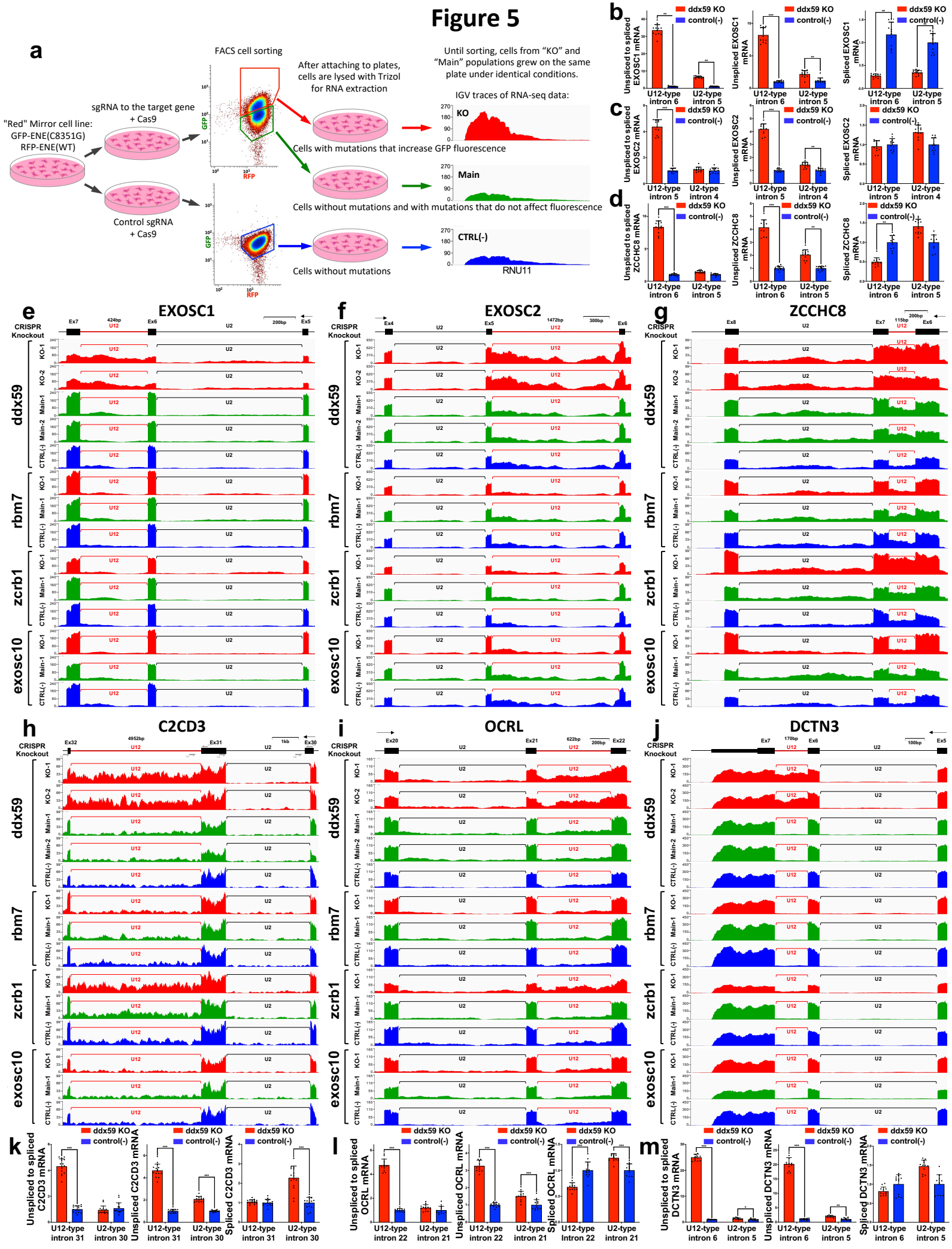
a
"Red" Mirror cell line:
GFP-ENE(C8351G)
RFP-ENE(WT)
sgRNA to the target gene
+ Cas9
Control sgRNA
+ Cas9
FACS cell sorting
GFP
RFP
After attaching to plates, cells are lysed with Trizol for RNA extraction
Cells with mutations that increase GFP fluorescence
Cells without mutations and with mutations that do not affect fluorescence
Cells without mutations
Until sorting, cells from "KO" and "Main" populations grew on the same plate under identical conditions.
IGV traces of RNA-seq data:
KO
Main
CTRL(-)
RNU11
b
c
d
ddx59 KO
control(-)
Unspliced to spliced EXOSC1 mRNA
Unspliced EXOSC1 mRNA
Spliced EXOSC1 mRNA
Unspliced to spliced EXOSC2 mRNA
Unspliced EXOSC2 mRNA
Spliced EXOSC2 mRNA
Unspliced to spliced ZCCHC8 mRNA
Unspliced ZCCHC8 mRNA
Spliced ZCCHC8 mRNA
U12-type intron 6
U2-type intron 5
U12-type intron 5
U2-type intron 4
e
EXOSC1
f
EXOSC2
g
ZCCHC8
CRISPR Knockout
ddx59
rbm7
zcrb1
exosc10
KO-1
KO-2
Main-1
Main-2
CTRL(-)
U12
U2
h
C2CD3
i
OCRL
j
DCTN3
k
Unspliced to spliced C2CD3 mRNA
Unspliced C2CD3 mRNA
Spliced C2CD3 mRNA
U12-type intron 31
U2-type intron 30
l
Unspliced to spliced OCRL mRNA
Unspliced OCRL mRNA
Spliced OCRL mRNA
U12-type intron 22
U2-type intron 21
m
Unspliced to spliced DCTN3 mRNA
Unspliced DCTN3 mRNA
Spliced DCTN3 mRNA
U12-type intron 6
U2-type intron 5

Figure 6

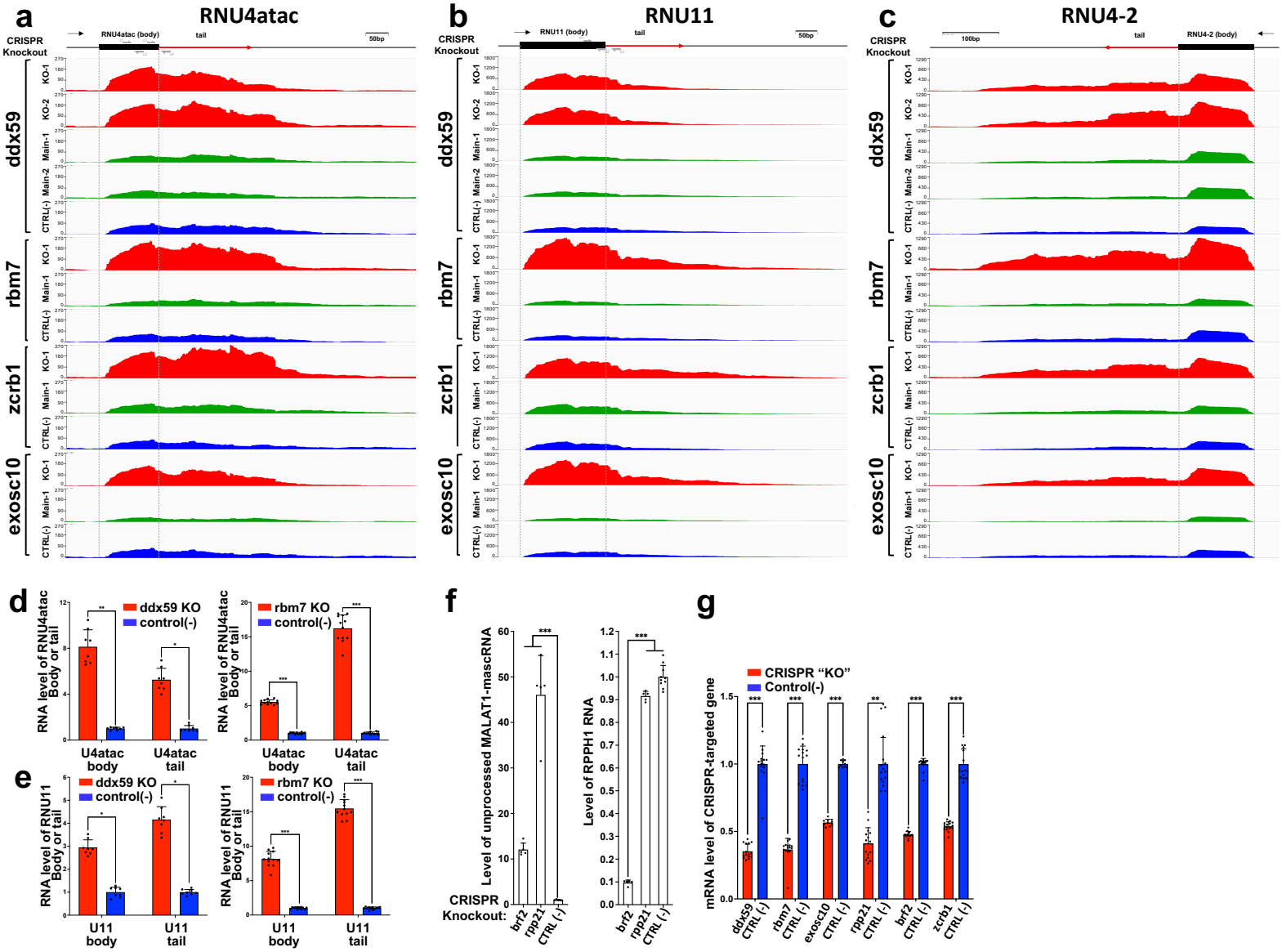
a
RNU4atac
b
RNU11
c
RNU4-2
CRISPR Knockout
RNU4atac (body)
tail
50bp
RNU11 (body)
100bp
RNU4-2 (body)
ddx59
rbm7
zcrb1
exosc10
KO-1
KO-2
Main-1
Main-2
CTRL(-)
d
ddx59 KO
control(-)
rbm7 KO
RNA level of RNU4atac Body or tail
U4atac body
U4atac tail
e
RNA level of RNU11 Body or tail
U11 body
U11 tail
f
Level of unprocessed MALAT1-mascRNA
Level of RPPH1 RNA
CRISPR Knockout:
brf2
rpp21
CTRL (-)
g
CRISPR "KO"
Control(-)
mRNA level of CRISPR-targeted gene
ddx59 CTRL (-)
rbm7 CTRL (-)
exosc10 CTRL (-)
rpp21 CTRL (-)
brf2 CTRL (-)
zcrb1 CTRL (-)